



The spatiotemporal variability of precipitation over the Himalaya: evaluation of one-year WRF model simulation

Jesse Norris¹ · Leila M. V. Carvalho^{1,2} · Charles Jones^{1,2} · Forest Cannon^{1,2} ·
Bodo Bookhagen³ · Elisa Palazzi⁴ · Adnan Ahmad Tahir⁵

Received: 9 September 2015 / Accepted: 17 October 2016 / Published online: 16 November 2016
© Springer-Verlag Berlin Heidelberg 2016

Abstract The Weather Research and Forecasting (WRF) model is used to simulate the spatiotemporal distribution of precipitation over central Asia over the year April 2005 through March 2006. Experiments are performed at 6.7 km horizontal grid spacing, with an emphasis on winter and summer precipitation over the Himalaya. The model and the Tropical Rainfall Measuring Mission show a similar inter-seasonal cycle of precipitation, from extratropical cyclones to monsoon precipitation, with agreement also in the diurnal cycle of monsoon precipitation. In winter months, WRF compares better in timeseries of daily precipitation to stations below than above 3-km elevation, likely due to inferior measurement of snow than rain by the stations, highlighting the need for reliable snowfall measurements at high elevations in winter. In summer months, the nocturnal precipitation cycle in the foothills and valleys of the Himalaya is captured by this 6.7-km WRF simulation, while coarser simulations with convective parameterization show near zero nocturnal precipitation. In winter months, higher resolution is less important, serving only

to slightly increase precipitation magnitudes due to steeper slopes. However, even in the 6.7-km simulation, afternoon precipitation is overestimated at high elevations, which can be reduced by even higher-resolution (2.2-km) simulations. These results indicate that WRF provides skillful simulations of precipitation relevant for studies of water resources over the complex terrain in the Himalaya.

Keywords WRF · Himalayas · Mesoscale · Precipitation · Climate change · Orographic precipitation · Water resources

1 Introduction

As Earth warms, both presently and in the future, water resources in different areas around the world are likely to be redistributed (e.g., Barnett et al. 2005; Scherler et al. 2011; Vano et al. 2014). Changes in moisture availability and precipitation patterns depend on the geography of affected areas. The fate of the water resources in regions with complex terrain such as High Asia will be governed by interactions between synoptic-scale and mesoscale flows and how these processes will distribute rain and snowfall in years to come.

In southern Asia, the Himalaya enhances and redistributes large-scale precipitation systems associated with winter storms, the monsoon, and other relevant weather systems (e.g., Lang and Barros 2004; Bookhagen et al. 2005; Barros et al. 2006; Bookhagen and Burbank 2010; Wulf et al. 2010; Medina et al. 2010; Norris et al. 2015). Different sub-regions within the Himalaya have different precipitation regimes and hence different influences in runoff. An east–west contrast in precipitation regime exists along the Himalayan arc (e.g., Bookhagen and Burbank 2010). Eastern drainage basins receive at least 70% of their annual precipitation in

✉ Jesse Norris
jesse.norris@ucsb.edu

¹ Earth Research Institute, University of California Santa Barbara, Santa Barbara, CA 93106, USA

² Department of Geography, University of California Santa Barbara, Santa Barbara, CA 93106, USA

³ Institute of Earth and Environmental Science, University of Potsdam, Karl-Liebknecht-Str. 24–25, 14467 Potsdam-Golm, Germany

⁴ Institute of Atmospheric Sciences and Climate, National Research Council, Corso Fiume 4, 10133 Torino, Italy

⁵ Department of Environmental Sciences, COMSATS Institute of Information Technology, Abbottabad, Pakistan

the summer from the Indian monsoon, predominantly as rain, which drains quickly after falling. Western drainage basins receive at least half their annual precipitation from extratropical cyclones in winter months, predominantly as snow, so that most of the runoff comes from snow and glacier melt in spring. There is considerable variability in climate projections between different sub-regions within south Asia (Immerzeel and Bierkens 2012; Kapnick et al. 2014). For example, the Coupled Model Intercomparison Project Phase 5 (CMIP5) models project that total precipitation will increase at a greater rate in the western Himalaya and Karakoram than in the central and eastern Himalaya in the second half of the twenty-first century (Kapnick et al. 2014). Although rainfall is projected to increase throughout the region, these studies indicate a neutral or slightly positive snowfall trend over western Himalaya and Karakoram but significant downward snowfall trend over central and eastern Himalaya. Furthermore, the projected changes in the vertical distribution of rain and snowfall over High Asia are geographically heterogeneous (Kapnick et al. 2014). In the central and eastern Himalaya, some snowfall will be replaced by rainfall at all elevations, while in the western Himalaya and Karakoram snowfall will decrease below 4000 m, but increase above 5000 m.

Despite these projections, considerable uncertainty exists regarding future precipitation over High Asia (Immerzeel and Bierkens 2012), partly because the mesoscale flow patterns arising from the complex terrain of High Asia cannot be resolved by climate models and partly because the future changes to the synoptic-scale flow patterns are unknown. The uncertainty in the projected changes in precipitation by climate models causes the largest uncertainty in future runoff and hence water availability in south Asia (Immerzeel et al. 2013; Lutz et al. 2014). Therefore, to predict how precipitation and hence runoff may change in and around the Himalaya, a clearer understanding of how various weather systems interact with the Himalaya is sought. If this can be accomplished, then the sensitivity of rain and snowfall in the region to future larger-scale climate change may be established.

Rain gauges are unevenly distributed over High Asia and the available observation-based gridded rainfall estimates (e.g., the Tropical Rainfall Measuring Mission, TRMM) are too coarse to capture orographic precipitation patterns. Moreover, reanalyses and even regional climate simulations are too coarse to capture these precipitation patterns, due to the poor representation of the complex topography of the Himalaya. Regional climate simulations over the Himalaya at about 50-km grid spacing have a wet bias at high elevations and a dry bias in the foothills (Ghimire et al. 2015). Because of these shortcomings of coarser simulations, great emphasis has been placed on mesoscale simulations at 10-km or smaller grid spacing (particularly with the Weather Research and Forecasting (WRF) model) to further our understanding about orographic precipitation, particularly

snowfall. In other high mountain ranges where observational networks are more expansive, e.g., the Rockies, precipitation patterns simulated by WRF have been shown to be highly accurate (Rasmussen et al. 2011). Therefore, over the Himalaya, where observational networks are less expansive, mesoscale simulations likely provide the most accurate available estimation of the mesoscale precipitation distribution.

Previous studies investigating the spatiotemporal distribution of precipitation in High Asia based on mesoscale simulations have generally focused on the Tibetan Plateau or in the Himalayan foothills, where stations for validation are more widespread and reliable. For example, Maussion et al. (2011) ran WRF over the Tibetan Plateau for 1 month when heavy rain and snow were observed and compared the output to station data. They found the model to be successful in the timing of precipitation, but simulated accumulations exceeded those of many the station measurements by a factor of 2–3. Li et al. (2009) also found a good agreement between WRF and observations over the Namco Lake on the Tibetan Plateau during a lake-effect snow event. Sato (2013) used WRF to simulate monsoon precipitation in the Meghalaya Plateau, in the foothills of the eastern Himalaya, and, although WRF was accurate in the timing of precipitation maxima over the course of a few weeks, the simulated onshore winds were too strong, resulting in excessive WRF precipitation. These studies illustrate the diverse abilities of high-resolution simulations for various weather systems over High Asia, but that model skill (in particular that of WRF) in simulating the observed precipitation varies with location and atmospheric conditions.

Most relevantly, Maussion et al. (2014) generated the High Asia Reanalysis (HAR), a 12-year dataset of WRF downscaling over High Asia at 10-km grid spacing, showcasing the inter-seasonal and inter-annual variability of flow patterns and precipitation in the region. When comparing mean station observations over the Tibetan Plateau to the nearest WRF grid points over 11 years, there was an excellent agreement, with WRF almost always within 10 per cent of the mean of the station measurements. However, that study did not assess the performance over the Himalaya. Over the Tibetan Plateau, the terrain is less heterogeneous than the Himalaya and so averaging observed and simulated measurements across large areas is reasonable. Over the Himalaya, on the other hand, precipitation magnitudes vary considerably within short distances (10s to 100s of km) and at different elevations as a result of convective, localized storms (Barros et al. 2006; Bookhagen and Burbank 2006). Thus, the reliability of mesoscale simulations to reproduce the true patterns of precipitation over the Himalaya remains poorly understood for the various weather systems affecting the region throughout the year. A comprehensive analysis of a model's ability to capture the actual spatiotemporal precipitation distribution over the

Himalaya over the course of the year at different grid spacings is therefore sought.

This study simulates a full year over the Himalaya at 6.7-km grid spacing to investigate WRF's ability to simulate the full annual range of mesoscale precipitation in the region. Although the HAR is available for 12 full years over roughly the same domain, the grid spacing in this study is small enough that convective parameterization may be switched off. Even over the Tibetan Plateau, Sato et al. (2008) found that 7-km grid spacing or less is required to simulate diurnal cycles of cloud formation. Over the more complex terrain of the Himalaya, smaller grid spacings lead to large improvements of near-surface temperature, and to a lesser extent precipitation, when compared to high-elevation stations (Collier and Immerzeel 2015). Like this study, Collier and Immerzeel (2015) performed a full year's WRF simulation over the Himalaya, but at higher resolution than in this study (their simulation used domains of 25, 5, and 1-km grid spacing) and with WRF interactively coupled to a glacier climatic mass balance model (WRF-CMB). However, their 5 and 1-km domains (those without parameterized convection) only spanned a small area within Nepal (their Fig. 1b). In contrast, the current study simulates a full year over the full Himalayan arc. This study investigates the differences in precipitation patterns between the HAR and the 6.7-km simulation in both winter and summer months, comparing them to available observations. However, because 6.7-km grid spacing does not in fact explicitly resolve convection and is at the coarse end of the scale of grid spacings for which convective parameterization may be switched off, shorter simulations at 2.2-km grid spacing are also presented to illustrate the potential improvements resulting from higher-resolution simulations over the Himalaya in both winter and summer.

Despite the many model studies over High Asia, there has yet to be a model study examining the interaction of various types of weather system with the full Himalaya on an interseasonal timescale, at resolution capable of simulating complex orographic precipitation patterns, and assessing the model's performance in doing so. This study examines the skill of WRF in representing local flows and precipitation variability over the course of a year, with focus on areas with steep slope in the Himalaya, where the region's most important rivers, including the Indus, Brahmaputra and Ganges, originate. A diverse set of observational data is used for comparison to the model over various sections of the Himalaya.

2 Model set up

Version 3.7.1 of the Advanced Research Weather Research and Forecasting (ARW-WRF, hereafter WRF) model

(Skamarock et al. 2008) was used to simulate one full year from 00 UTC 1 April 2005 to 00 UTC 1 April 2006. The year was simulated from April through March, as opposed to a full calendar year, in order to simulate a full winter season and a full summer season. The synoptic background and justification for this particular 12-month period are given in Sect. 4. The nested domains of 20 and 6.7-km grid spacing shown in Fig. 1a, b were configured with 50 vertical levels (nearly double the number used for the HAR) up to 50 hPa and the spatial domains were chosen to avoid intersection with the main topographic features. Unlike the HAR, the model was run continuously for the full 12 months (in that study, the model was re-initialized daily). In the current study, the model was initialized at 00 UTC 1 March, with the initial March's output discarded as model spin up, hence 12 months of retained output.

Climate Forecast System Reanalyses (CFSR, Saha et al. 2010) from the National Oceanic and Atmospheric Administration (NOAA)'s National Centers of Environmental Prediction (NCEP) were used at 0.5° (pressure levels) and 0.31° (surface variables) lat–lon grid spacing for initial and lateral boundary conditions. Evaluation of different reanalysis datasets has been performed by previous studies over the Tibetan Plateau, which for the current study is the most relevant area for reanalysis evaluation (since global reanalyses cannot be expected to be accurate over the complex terrain of the Himalaya). Bao and Zhang (2013) found CFSR and the Interim European Centre for Medium-Range Weather Forecasts (ECMWF) Re-Analysis (ERA-Interim) to compare best to sounding data over the Tibetan Plateau, indicating that these two are the most accurate reanalyses in simulating the three-dimensional structure of the atmosphere over High Asia. However, Maussion et al. (2014) tested ERA-Interim as initial and boundary conditions for WRF simulations, and found less agreement to in-situ precipitation observations than for the NCEP Global Forecasting System (GFS) that was used for the HAR. No testing of alternative initial and boundary conditions was performed for the current study and it is possible that otherwise-equivalent simulations forced by different reanalyses may compare better to observations than shown in this paper.

The parameterization schemes employed in these simulations are given in Table 1. Experiments were performed for a few days at a time, both during winter storms and the monsoon, to test the model's configuration. In these experiments, various boundary-layer, microphysics, and cumulus (outer domain only) schemes were performed, changing just one parameterization scheme from those in Table 1 per experiment. Subtle differences were evident between simulations in the distribution and intensity of precipitation in the mountains, but consistent with Maussion et al. (2011) no single scheme consistently outperformed all others.

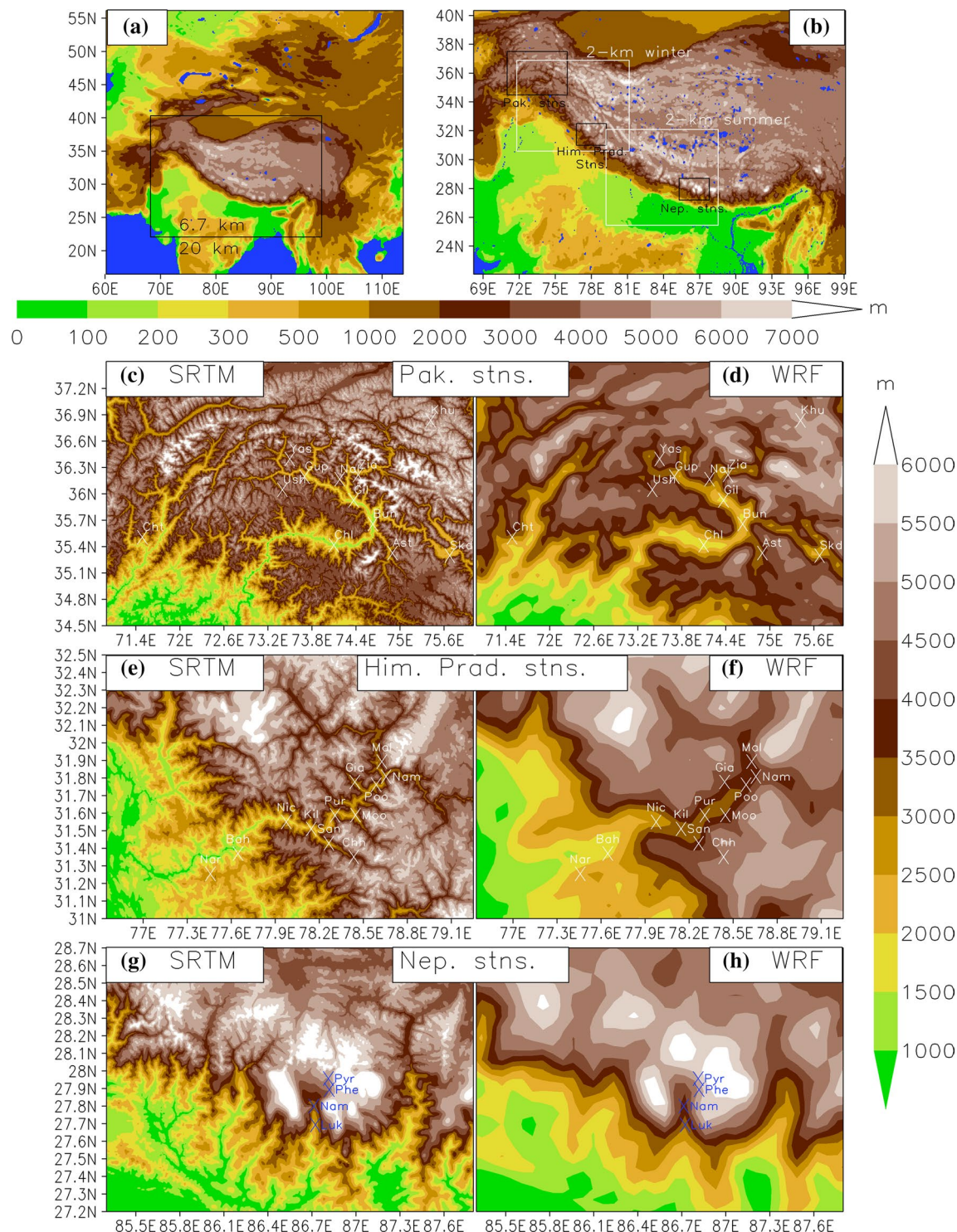


Fig. 1 **a, b** The two model domains at 20 and 6.7-km grid spacings, mapped with a Mercator projection, showing elevation in each domain. Blue indicates water bodies. In the inner domain (**b**), the domains at 2-km grid spacing mapped for separate 6-day simulations in winter and summer are shown, as well as the areas in which the

locations of the surface stations in Pakistan, Himachal Pradesh, and Nepal are shown in *panels (c–h)*, on the <1-km SRTM (left panels) and 6.7-km WRF (right panels) grids. The full names and elevations of the stations are given in Table 2. Note different color scale between *top row* and *bottom 3 rows*

Table 1 Parameterizations employed in the WRF simulation

Microphysics	Thompson et al. (2008)
Surface layer	MM5 Monin and Obukhov (1954)
Land surface	Noah-MP (Niu et al. 2011)
Longwave radiation	RRTMG (Iacono et al. 2008)
Shortwave radiation	RRTMG shortwave (Iacono et al. 2008)
Boundary layer	Yonsei University (Hong et al. 2006)
Cumulus	Kain (2004, outer domain only)

Dimri and Chevaturi (2014) found that the Eta microphysics scheme consistently had smaller precipitation errors when compared to observations than other schemes in the simulation of winter storms over the Himalaya, but the more sophisticated Thompson scheme employed in the current study was not tested.

Unlike the boundary-layer, microphysics, and cumulus schemes, WRF is highly sensitive to the choice of land-surface model (LSM) over the Himalaya, due to the different treatment of snowpack between schemes. Thomas et al. (2014) showed that the choice of LSM in WRF markedly changes circulation patterns in the lower troposphere over the Himalaya. This is relevant for the current study, since this may affect the orientation, location, and magnitude of moisture transport into the mountains. This study employs the Noah-MP LSM, which more accurately simulates terrestrial moisture processes and the evolution of snowpack on the timescale of months than other LSMs (Niu et al. 2011). To test sensitivity to spin-up of the Noah-MP LSM, a two-year simulation was also performed. This simulation was initialized on 00 UTC 1 April 2004, otherwise identical to that analyzed in this paper, and the final 12 months (April 2005 through March 2006) compared to the same 12 months in the simulation presented in this paper (i.e., comparing one month of spin-up to one year of spin-up). There was much more snowpack in the simulation with a year of spin up and consequently some differences in circulation and precipitation magnitudes from month to month (both in the mountains and over the plains). However, all the same precipitation features described in the current study over the Himalaya were also exhibited in the simulation with a year of spin up, and the conclusions of this study were not impacted. The two-year simulation is not presented.

Spectral nudging (Stauffer and Seaman 1990; Stauffer et al. 1991) of zonal and meridional wavenumbers 1–5 and 1–4, respectively, was applied to temperature, winds, and geopotential height in the outer domain at all vertical levels, to keep the inner domain as close to the reanalyses as possible. Sensitivity tests were performed for spectral and grid nudging with no qualitative or significant quantitative differences in the precipitation distribution. Switching off

the nudging altogether, however, resulted in spurious precipitation features and generally more intense precipitation in the mountains.

WRF output was saved every 3 h to showcase diurnal cycles and to compare with TRMM data (see Sect. 3). Because of the known wet bias over the Himalaya in regional climate simulations, it is uncertain whether the grid spacing employed in this study is small enough to overcome the shortcomings of coarser simulations. In particular, 6.7 km is a large grid spacing if switching off convective parameterization. To test whether 6.7 km is too large to simulate the orographic processes of interest, additional simulations were also performed with a 2.2-km domain nested within the 20 and 6.7-km domains. Because of the greater computational cost of a higher-resolution domain, these simulations were performed for just 6 days during the year simulated in this paper, one during winter and one during summer. The winter simulation was from 12–18 January 2006 (initialized at 00 UTC 12 Jan), when the full-year simulation showed extreme precipitation at high elevations associated with the passage of an extratropical cyclone. The summer simulation was from 16–22 July 2005 (initialized at 00 UTC 16 Jul) when the full-year simulation showed a diurnal monsoon pattern in the mountains that was representative of the summer. Different 2.2-km domains were nested for the winter and summer simulations, as shown in Fig. 1b. These locations were chosen according to where the precipitation of interest was distributed in each case, according to the full-year simulation. For both of these simulations, the model configuration was identical to that of the full-year simulation, with the 2.2-km domains using all the same options as the 6.7-km domain.

3 Observations and gridded estimates of precipitation used for comparison to model output

In this study, the WRF output is compared to three sets of surface stations, in the central and western Himalaya (Fig. 1b). For each set of stations, the locations are shown on <1-km resolution terrain represented by the Shuttle Radar Topography Mission (SRTM) topography and on the WRF grid, where the center of the “X” marks the precise location. The station elevations are given in Table 2.

The first set of stations is in Pakistan, with stations operated by the Pakistan Meteorological Department (PMD) and the Pakistan Water and Power Development Authority (WAPDA) in the western Himalaya and Karakoram, ranging from 1250–4440 m elevation. These stations record various daily meteorological variables, but in this study only precipitation is used. The locations of these stations

Table 2 Surface stations employed in this study

	Chilas	Bunji	Gilgit	Chitral	Gupis	Astore	Skardu	Naltar	Ziarat	Ushkore	Yasin	Khunjerab
Pakistan stations												
Shorthand	Chl	Bun	Gil	Cht	Gup	Ast	Skd	Nal	Zia	Ush	Yas	Khu
Elevation (m)	1250	1372	1479	1498	2156	2168	2210	2898	3020	3051	3280	4440
Operated by	PMD	PMD	PMD	PMD	PMD	PMD	PMD	WAPDA	WAPDA	WAPDA	WAPDA	WAPDA
	Kilba	Nichar	Bahli	Purbani	Moorang	Narkandar	Pooh	Sangla	Namgia	Giabong	Rakchham	Chhitkul
												Malling
Himachal Pradesh stations												
Shorthand	Kil	Nic	Bah	Pur	Moo	Nar	Poo	San	Nam	Gia	Rak	Chh
Elevation (m)	1938	2189	2249	2499	2545	2668	2699	2740	2831	2941	3046	3462
Operated by	BBMB	BBMB	BBMB	BBMB	BBMB	BBMB	BBMB	BBMB	BBMB	BBMB	BBMB	BBMB
	Lukla		Namche		Pheriche		Pyramid					
Nepal stations												
Shorthand	Luk		Nam		Phe		Pyr					
Elevation (m)	2660		3570		4260		5035					
Operated by	Ev-K2-CNR		Ev-K2-CNR		Ev-K2-CNR		Ev-K2-CNR					

PMD Pakistan Meteorological Department, WAPDA Pakistan Water and Power Development Authority, BBMB Bhakra Beas Management Board

are shown in Fig. 1c, d in the area indicated in Fig. 1. As shown on the SRTM grid, the stations gradually wind up the Indus and Hunza valleys (the confluence where Bunji (Bun) is located is where the Hunza rises to the northwest and the Indus rises to the southeast), while some are on nearby slopes or in nearby valleys. The measurements from PMD and WAPDA stations have been successfully used in previous studies to characterize various meteorological and hydrological features of the western Himalaya and Karakoram—for example, the inter-annual variability of precipitation (Archer and Fowler 2004), the relationship of summer temperatures and runoff (Fowler and Archer 2006), the annual cycle of precipitation (Palazzi et al. 2015), and the relationship between precipitation and glacier mass balance in the area (Tahir et al. 2011).

The second set of stations is in Himachal Pradesh, northwest India, operated by the Bhakra Beas Management Board (BBMB), ranging from 1938–3588 m. These stations distinguish between rain and snowfall, as detailed in Bookhagen et al. (2005) and Wulf et al. (2010). The locations of these stations on the SRTM and WRF grids are shown in Fig. 1e, f, in the area indicated in Fig. 1b (elevations in Table 2), as they rise up the Sutlej valley and its tributaries.

The third set of surface stations used in this study is the Stations at High Altitude for Research on the Environment (SHARE, <http://www.ev2cnr.org/cms/en/share/project/intro>) network in Nepal, operated by Ev-K2-CNR, ranging from 2660–5035 m. The locations of these stations are shown

in Fig. 1g, h in the area indicated in Fig. 1b (elevations in Table 2). See Ueno et al. (2008) for a comprehensive description of the station locations and Bonasoni et al. (2008) for details of the Pyramid measuring site. These stations record hourly data, which was aggregated to 3-h data to match the frequency of WRF output, allowing for comparisons to the simulated diurnal cycle. For these stations, temperature, meridional wind speed, specific humidity, and incoming shortwave radiation were also used.

For all three sets of stations, rainfall is measured with a tipping bucket and (in the case of the stations in Himachal Pradesh only) snowfall is converted from snow depth and density measurements into snow water equivalents. As noted by Ueno et al. (2008), a tipping bucket does not record snowfall until it melts. There is therefore a delay of a few hours or more in some of the precipitation measurements, particularly in the winter, with increasing elevation, and at nighttime. Furthermore, much of the precipitation that falls is blown out of the gauge or does not fall in the gauge at all, particularly at the more exposed (i.e., higher-elevation) stations, as noted by Bollasina et al. (2002). This is a particular issue with snow, which almost all winter precipitation is at these high elevations. In the summertime, this is likely to be less of an issue because most high-elevation precipitation falls as rain and winds are weaker. In the winter, however, as explained by Tahir et al. (2011) regarding the stations in Pakistan, the highest-altitude stations only catch 20–30% of precipitation. In winter, the PMD and WAPDA stations in Pakistan suggest a climatological

precipitation maximum at about 3000 m (Palazzi et al. 2015), when in reality the maximum is at about 5000 m (Hewitt 2014), illustrating the undercatch at the highest-elevation stations. As will be shown, this leads to very large discrepancies between simulated precipitation and observations at high elevations during winter months. Thus, we refrain from drawing conclusions from the stations in terms of the vertical distribution or intensity of precipitation. The station measurements are not perfect, but are the best available high-elevation stations in the region. As will be shown, they are useful in the wintertime for comparing to the model's timing of winter storms. In the summertime, the stations in Nepal are useful for comparison to the model's diurnal cycle.

For all three sets of stations, although not resolving the subtleties of the terrain, the 6.7-km WRF grid mostly captures where the stations are distributed, relative to the terrain (Fig. 1). However, there are subtle differences between WRF and SRTM in terms of how high up a peak or how far down in a valley stations are, leading to differences in elevation between the stations' true locations and the nearest WRF grid point. Comparisons are also made in this paper between the HAR at 10-km grid spacing and station measurements. Therefore, comparisons between the station measurements and the nearest point on the WRF grid were not considered to be representative. Instead, for each station, the mean WRF precipitation was taken of at least 10 grid points within a radius of 10 grid points (66.7 km, or, in the case of the HAR, 100 km) of the station's true co-ordinates that were within a certain range of the station's true elevation. If at least 10 grid points within the given radius were within 100 m of the station's true elevation, then the mean precipitation was taken from these grid points. Otherwise, the elevation range was increased by 100 m until 10 grid points were found and the mean precipitation or other variable was taken from the grid points identified. No stations required an elevation range of more than 400 m. The justification for this method was an attempt to search a small number of grid points as close as possible to the station's true elevation. Requiring grid points to have similar aspect and slope to the station locations did not change the results markedly.

TRMM 3B42V7 (Huffman et al. 2007) (TRMM) was used for comparison to WRF's precipitation distribution over High Asia, and to evaluate the inter-seasonal and diurnal evolution of model precipitation. TRMM is available on a $0.25^\circ \times 0.25^\circ$ lat–lon grid (50°S – 50°N ; 0 – 360°W). The product is obtained by combining infrared and microwave data from multiple satellites to estimate precipitation rates every three hours. Station data is used for bias correction.

Because TRMM is itself an estimate of precipitation distribution, we do not present it as a validation of WRF, particularly because TRMM is unreliable in estimating

snowfall (e.g., Lang and Barros 2004; Barros et al. 2006; Anders et al. 2006), which is of primary interest to this study. While we acknowledge TRMM's limitations, as discussed in the introduction, it is the most reliable decadal dataset of gridded-precipitation estimates in the Himalaya that is independent of model simulations. However, due to the shortcomings of TRMM, the Moderate Resolution Imaging Spectroradiometer (MODIS) Cloud Mask product (http://modis-atmos.gsfc.nasa.gov/MOD35_L2/) is also used in this study for validation of WRF's cloud-cover distribution. These data are obtained from visible imagery from the daily passes of the Terra (which passes over High Asia at about 5 UTC) and Aqua (which passes over High Asia at about 8 UTC) satellites.

The APHRODITE (Yasutomi et al. 2011; Yatagai et al. 2012) precipitation dataset, generated by interpolating available surface station data, was also considered. However, this data set is mostly based on low-elevation stations, hence is useful on the plains, but not for the high elevations of interest in this study. The distribution of high-elevation stations contributing to the data changed a great deal over the course of the year, implying an inconsistency in the product. APHRODITE was therefore not used in this study as it was not deemed a reliable dataset for comparison to the model over the given year.

4 Overview of atmospheric conditions during April 2005–March 2006

The particular year simulated in the current study was characterized by the negative phase of the El Niño Southern Oscillation (ENSO) with intraseasonal variability associated with the Madden–Julian Oscillation (MJO). A weak La Niña event occurred in the winter (<http://ggweather.com/enso/oni.htm>), which is associated with reduced winter precipitation over the Himalaya (Cannon et al. 2016). However, strong extratropical cyclones do still deposit large amounts of precipitation in La Niña years, including in March 2006 (Norris et al. 2015), which is within the year simulated in this study. A 45-day MJO event of about average amplitude occurred through January and early February, according to the Jones (2009) index. This MJO event included enhanced convection over both the Indian Ocean/Maritime Continent and western Hemisphere, associated with widespread descent and ascent, respectively, over southwest Asia (Barlow et al. 2005). However, both these MJO phases can enhance winter precipitation in the western Himalaya and Karakoram by differing mechanisms (Cannon et al. 2016). This summer was only slightly below average in monsoon intensity, but almost as close to an average monsoon as has occurred since 1979, according to the Large-Scale Index for the Indian Monsoon (LIMS,

Carvalho et al. 2016; their Fig. 7). The June–September All India Monthly precipitation, obtained from the Indian Meteorological Department (<http://www.imd.gov.in/>) indicated that the 2005 monsoon season was nearly average (−1.3% departure from the mean). However, precipitation was not uniformly distributed throughout the wet season. The early part of the monsoon season was anomalously dry (−9.5% departure from the mean in June), transitioning to wet conditions in July (+14.72% departure from the mean). Dry conditions prevailed again in August (−28%) while rainfall was above normal in September (+20%).

To offer some perspective on each month investigated in this study, monthly CFSR (first and third columns) and TRMM (second and fourth columns) anomalies are shown in Fig. 2. Most anomalies were short-lived and there were not many consecutive months with the same anomaly, indicating that large departures from average conditions generally did not persist anywhere over south Asia for prolonged parts of the year. The only exception was a prolonged dry anomaly (low precipitable water) over northern India from April to June (Fig. 2, CFSR panels). Correspondingly, the TRMM panels in Fig. 2 show that there was anomalously low precipitation over the Himalaya during these months. In particular, a low-moisture anticyclonic anomaly over northern India occurred in June, associated with a negative precipitation anomaly shown by TRMM. These synoptic features explain the anomalous dry pre-monsoon period. July and August, the core monsoon months, were closer to average, although there was a dry (low precipitable water) anti-cyclonic anomaly over northern India in August with an associated dry (low precipitation) anomaly in TRMM over part of the Himalaya. However, there was not a sustained dry or wet anomaly in any particular area through the summer.

A moist cyclonic anomaly in September (Fig. 2, CFSR panel), is due to a series of tropical cyclones (as illustrated by individual CFSR reanalyses, not shown), with the corresponding TRMM panel showing the consequent wet anomaly along parts of the western Himalaya. Because of the very different physical processes between the monsoon and tropical cyclones, September is excluded from the analysis of the monsoon in Sect. 7.

The winter contained mostly negative precipitable-water anomalies near the western Himalaya (where most winter precipitation falls in the region), likely due to the La Niña episode, although these were very weak compared to positive and negative anomalies in most other years. According to TRMM, this winter's precipitation anomalies over the western Himalaya were mostly negative, but the anomalies for the total winter were as close to zero as any other year in the TRMM data period (not shown). March shows positive precipitation anomalies due to the strong extratropical cyclone discussed above and so March is included in the analysis of

winter in Sect. 6. As discussed, TRMM is deficient in detecting snowfall, and the HAR in fact shows a slightly positive anomaly at high elevations in the western Himalaya and Karakoram for total winter precipitation (not shown).

Considering both summer and winter circulation and large-scale precipitation in the region, this year simulated was as close to average as possible in the region during years for which all observational data used in this study were available (2003 onward).

5 Inter-seasonal evolution of precipitation distribution across the Himalaya

This section provides an overview of the inter-seasonal evolution of the precipitation distribution over the Himalaya from April 2005 through March 2006, comparing WRF to observational data on a month-by-month basis. Comparisons are also made between the model configuration in the current study (6.7-km grid spacing with no convective parameterization) and the HAR (10-km grid spacing with convective parameterization) to gauge what model setup is necessary to simulate accurately different times of year over the Himalaya.

Figure 3 shows the monthly accumulated precipitation from WRF from April 2005 through March 2006, together with the differences between WRF and TRMM, and the spatial correlation of total precipitation each month between WRF and TRMM. WRF simulates the annual cycle of precipitation over the Himalaya, with a correlation most months of above 0.6 with TRMM, as follows.

In April and May (pre-monsoon), a stratiform precipitation maximum lies over the eastern Himalaya and over low elevations, associated with moisture advection from the Bay of Bengal. In April there is little orographic enhancement, but as summer progresses a band of enhanced precipitation develops over the eastern Himalaya and gradually extends further west. By July, widespread monsoon rain falls over the Gangetic Plain (south of the Himalaya) with a near-continuous band of enhanced precipitation along the full Himalayan ridge and lighter (about 10% of the magnitude) but widespread precipitation over the Tibetan Plateau. In winter months, precipitation is confined to the western Himalaya and the highest elevations in conjunction with extratropical cyclones. As winter progresses, the band of orographic precipitation extends further east along the Himalaya.

All the precipitation features described above, are also exhibited by the HAR's 12-year climatology (see Fig. 2 of Maussion et al. 2014 and Fig. 6 of Curio et al. 2015), indicating that the year simulated in the current study is representative of the climatology. Curio et al. (2015) also showed the climatology of moisture transport for each

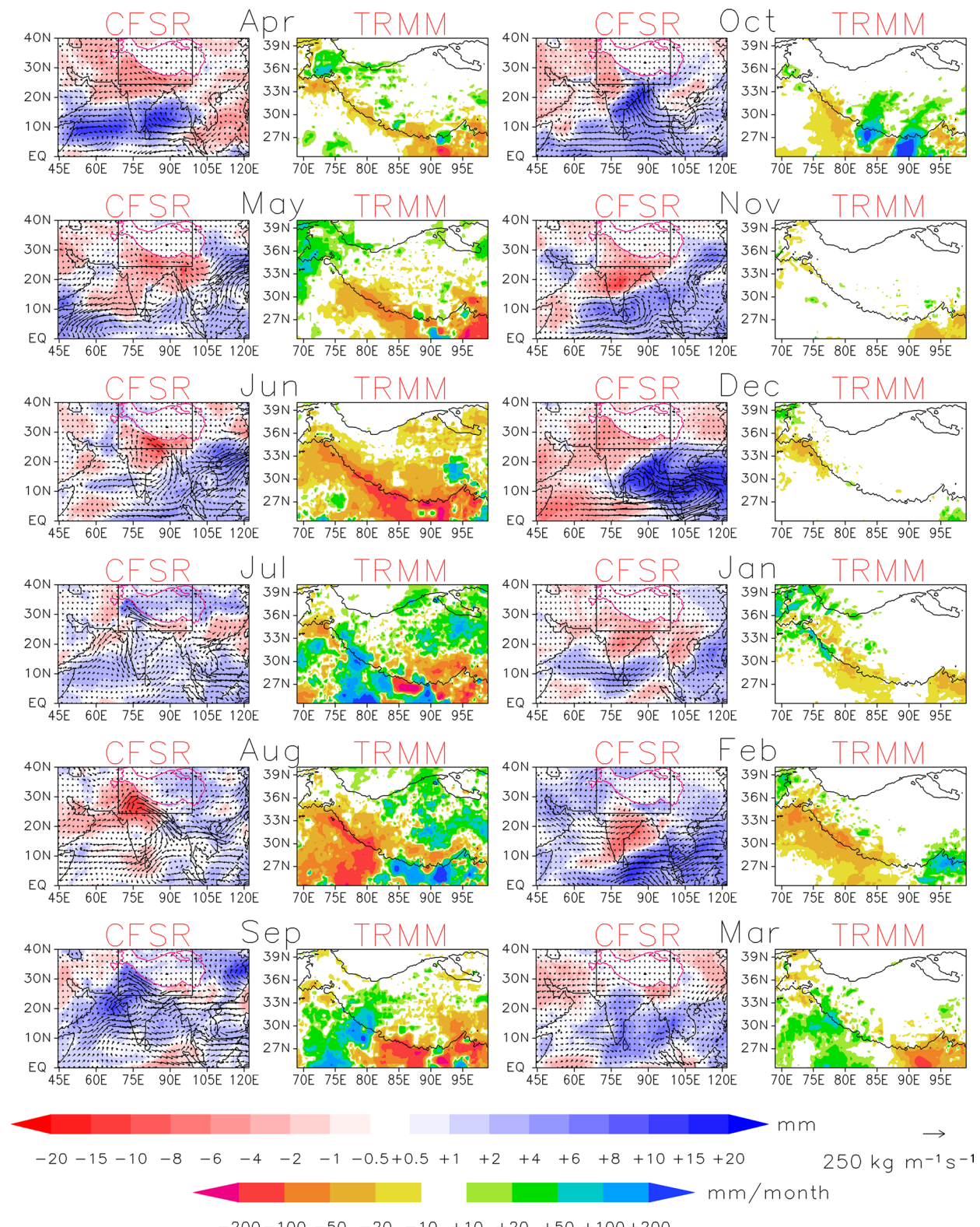


Fig. 2 Monthly anomalies from April 2005 through March 2006 from the 1979–2013 CFSR (first and third columns) and 1998–2012 TRMM (second and fourth columns) climatologies. CFSR panels show precipitable water (mm, blues positive, reds negative) and vec-

tors of column-integrated moisture transport ($\text{kg m}^{-1}\text{s}^{-1}$). TRMM panels show precipitation (colors, mm). All panels also show the 3-km elevation contour in bold, indicating the location of High Asia. The area shown in TRMM panels is indicated in CFSR panels

calendar month (their Fig. 4), which very closely resembles that of the simulation in the current study (not shown). Therefore, the HAR at 10-km grid spacing is sufficient to investigate the climatology of precipitation and drivers of precipitation, and with 12 years of data can also showcase interannual variability, as shown in Maussion et al. (2014). However, by zooming into sub-regions within the domain, important differences in precipitation exist for this 12-month period between the HAR and the simulation in the current study (Fig. 4).

The distribution of accumulated precipitation in DJFM over the western Himalaya and Karakoram, where almost all precipitation fell in this winter, is very similar between the HAR and the 6.7-km simulation (Fig. 4, top row). In both cases, the distribution is almost entirely defined by elevation, with all the same precipitation features morphologically very similar between both simulations, albeit with slightly less detail in the HAR, due to the coarser topography. In both simulations there is a maximum of total winter precipitation between 5000 and 5500 m elevation (only slightly decreasing with elevation above 5500 m) (not shown), consistent with Hewitt (2014) who states the level of maximum winter precipitation over the Himalaya to be about 5000 m. Furthermore, the magnitudes of precipitation maxima are similar between the two, with the maxima in the 6.7-km simulation just a few hundred mm greater than in the HAR, likely due to slightly steeper terrain and hence stronger updrafts. The breakdown between rain and snow is also almost identical (not shown). Given all the other differences in model configuration between the HAR and the simulation in this study (GFS vs. CFSR forcing, the number of vertical levels, the daily reinitialization of the HAR, various different parameterizations), the similarity of the two simulations' precipitation distribution implies a very low sensitivity of simulated winter precipitation over the Himalaya to model configuration.

A simulation at 2.2-km grid spacing was also performed during this winter (see Sect. 2) over the area shown in Fig. 1b ("2-km winter" box), which is the area plotted in the top row of Fig. 4. There was no meaningful difference between the 6.7 and 2.2-km domains in the distribution and negligible difference in the magnitude of maxima (not shown). As with the 6.7-km domain, the precipitation distribution was almost entirely defined by elevation, but showing finer-scale features, due to the more complex topography at the higher resolution. Due to the complexity of the terrain in the Himalaya, any reduction in grid spacing may be made to investigate finer-scale flow and precipitation patterns. However, these simulations show that for winter precipitation, little meaningful difference is made from 10 km to lower grid spacings. From a hydrological perspective, including the breakdown between rain and

snow, this result implies that the HAR may be used to estimate water resources from winter precipitation virtually as well as higher-resolution simulations.

Conversely, in summer months, the 6.7-km simulation shows 1000–1500 mm greater seasonal accumulation than the HAR, both in the foothills (roughly 1000–3000 m elevation) and over the Himalayan peaks (north of the 3000-m elevation contour) (Fig. 4, bottom row). The area shown is roughly that covered by Nepal, but other sub-regions within the domain show similar differences. This difference between the simulations means that the 6.7-km simulation overestimates summer precipitation, while the HAR underestimates summer precipitation at high elevations, according to the Nepal stations (Fig. 5). The stations, the HAR, and the 6.7-km simulation all show that summer precipitation at Lukla (which at 2660 m may be considered to be in the foothills) is much greater than at the higher-elevation stations. This result is consistent with the findings of Putkonen (2004), namely that there is a maximum of monsoon precipitation at about 3000 m in the central Himalaya. However, at all stations, the HAR generally only shows about half of the station-measured monthly totals, while the 6.7-km simulation generally shows 1.5–2 times the station-measured amounts. Unlike with winter precipitation, the difference in magnitude between the two simulations is not a simple case of the same precipitation features existing in both but of lower magnitude in the HAR, as will be shown in Sect. 7.

6 Daily winter precipitation

This section focuses on whether WRF is accurate in reproducing the timing, intensity, and coverage of winter daily precipitation. This analysis is performed in the western Himalaya and Karakoram, where the vast majority of the winter precipitation falls (Fig. 3).

To investigate the accuracy of WRF's winter precipitation distribution at a finer scale than TRMM is available for comparison, satellite and station data are now used for comparison to WRF's winter snowfall over the western Himalaya and Karakoram. Due to the shortcomings of high-altitude surface stations discussed previously, satellite cloud-cover data from MODIS (Sect. 3) are now compared to those of WRF as a proxy for precipitation amount. Figure 6 shows the daily correlation from December through March of total cloud fraction between WRF and MODIS. Each MODIS pixel is correlated in time with the coarser WRF grid point in which it lies (i.e., the figure is at MODIS resolution). This figure illustrates that over this region, WRF is reasonably accurate at the timing of cloud cover, with large areas attaining a correlation coefficient of more

Table 3 Precipitation comparisons between WRF and surface stations in Pakistan and Himachal Pradesh in winter months

	Chl	Bun	Gil	Cht	Gup	Ast	Skd	Nal	Zia	Ush	Yas	Khu	
Pakistan stations													
Elevation (m)	1250	1372	1479	1498	2156	2168	2210	2898	3020	3051	3280	4440	
Stn. total (mm)	72	35	24	215	27	216	142	213	30	52	81	37	
WRF total (mm)	142	136	140	278	130	115	79	199	200	267	163	200	
r	0.57	0.81	0.45	0.60	0.16	0.58	0.63	0.28	0.21	-0.13	0.37	0.38	
	Kil	Nic	Bah	Pur	Moo	Nar	Poo	San	Nam	Gia	Rak	Chh	Mal
Himachal Pradesh stations													
Elevation (m)	1938	2189	2249	2499	2545	2668	2699	2740	2831	2941	3046	3462	3588
Stn. total (mm)	576	418	143	219	307	103	86	201	126	197	344	437	62
WRF total (mm)	186	216	224	236	254	293	305	264	323	330	321	367	367
r	0.53	0.65	0.29	0.69	0.57	0.40	0.22	0.38	0.48	0.57	0.72	0.82	0.45

The given values for WRF and the stations are the accumulations from 1 Dec 2005 through 31 Mar 2006. The given “r” values are the Pearson product-moment correlation coefficients of times of daily precipitation between WRF and the stations over the same period

than 0.6 between WRF and MODIS. The correlation is generally worse, however, over the Karakoram (the northeastern part of the area shown). Therefore, WRF is accurate in the timing of winter storms on the windward slopes of the Himalaya, but the more complex flow patterns forming further into the mountains are not so well represented by the model.

To relate this local variability of winter cloud cover to local variability of precipitation, Table 3 shows the accumulation through winter at each of the stations in Pakistan and Himachal Pradesh, according to both the station measurements and WRF (using the method of finding appropriate grid points detailed in Sect. 3 for each station location), as well as the correlations of daily precipitation. The comparisons of total winter precipitation are highly variable between stations, with some showing about the same amounts between WRF and the stations and some showing more than 5 times more according to WRF than the station. Likewise, the correlations of the timeseries of daily precipitation through winter vary between 0.82 and -0.13, although most are above 0.4. Given the highly heterogeneous spatial precipitation patterns arising from the complex terrain, as well as the errors that may occur with both the model and the stations, comparisons are difficult between the model and individual stations located on the order of 10 km apart.

Averaging over stations below and above 3-km elevation separately, and, for WRF, grid points below and above 3 km, generates more meaningful comparisons (Fig. 7). For the lower-elevation timeseries, WRF is averaged over all grid points below 3 km, but above the elevation of the lowest station, within the areas shown in Fig. 1. For the high-elevation timeseries, WRF is averaged over all grid points above 3 km, but below the elevation of the highest station.

Separate timeseries are shown for the stations in Pakistan and Himachal Pradesh, where WRF is averaged over all grid points in the given elevation range within the areas shown in Fig. 1d, f, respectively. Constructing equivalent time series for the HAR shows no meaningful difference to the 6.7-km WRF timeseries shown (just slightly lower daily values, not shown), further illustrating the sufficiency of the HAR for simulating winter precipitation.

WRF and the stations both show that precipitation is more frequent in the area containing the Pakistan than Himachal Pradesh stations (Fig. 7). This is because the Pakistan stations are more within the area of maximum winter precipitation (Fig. 3). However, certain storms that lead to the largest accumulations in Pakistan also generate large accumulations in the mountains in Himachal Pradesh (in particular those between 30–35 days and 40–50 days).

The station measurements and WRF are generally well correlated for daily precipitation. However, for the Pakistan stations, there is a large difference between low- (correlation of 0.78) and high-elevation (correlation of 0.41) stations (Fig. 7, left panels). At low elevations (<3 km) in Pakistan, there is almost never a day in which precipitation was recorded at the stations, but not simulated by WRF at the given location (or vice versa). This was also the case in the daily winter-precipitation timeseries of Collier and Immerzeel (2015) when averaging across stations (their Fig. 3a). Also, the heaviest days of precipitation shown by WRF are also the days on which significant precipitation was recorded by the stations. Hence, there is a correlation of 0.78 in the daily timeseries, although WRF shows nearly three times the total winter accumulation as the stations. At high elevations (>3 km) in Pakistan, although WRF and the stations agree that precipitation was more frequent through the winter than below 3 km, the comparison is

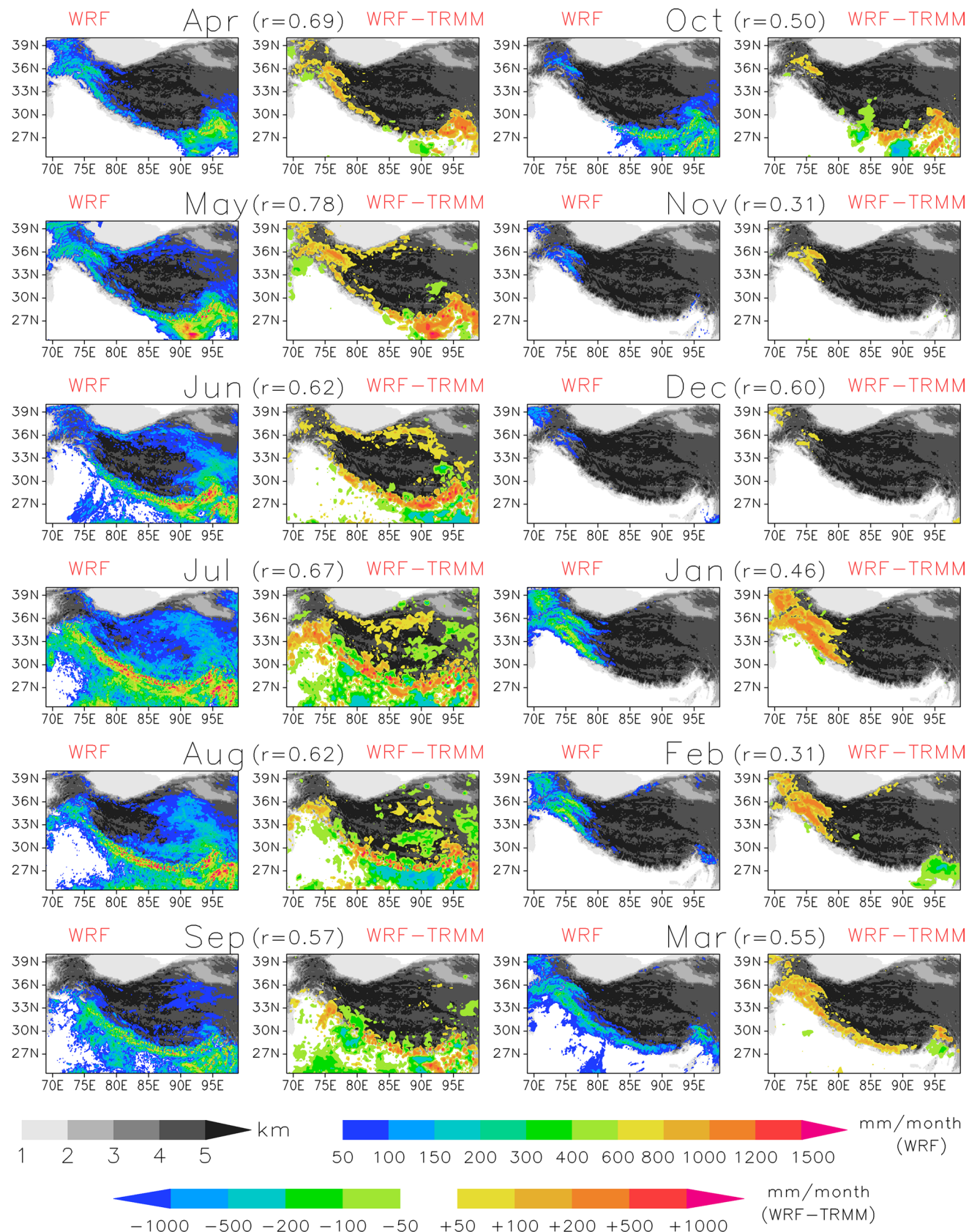


Fig. 3 First and third columns: The total WRF precipitation (colors, mm) falling in the inner domain each month from April 2005 through March 2006. Second and fourth columns: TRMM total precipitation each month over the same area, subtracted from the WRF monthly total (bilinearly interpolated onto the coarser TRMM grid). The given “r” values are, for each month, the Pearson product-moment correlation coefficient of the spatial distribution of total precipitation between TRMM and interpolated WRF, indicating the level of agreement between WRF and TRMM each month over the area covered by the inner WRF domain. Also plotted in all panels is elevation (grays, km)

much poorer. WRF shows nearly ten times the accumulation shown by the stations and there is less agreement about which days were the heaviest.

For the stations in Himachal Pradesh, which measure rain and snow separately, the comparisons between WRF and the stations are much better than for the Pakistan stations, both below and above 3 km (cf. left and right panels of Fig. 7). Above 3 km in Himachal Pradesh, the WRF total for winter is less than double that of the stations (Fig. 7, bottom right) (as opposed to ten times the station total in the case of the Pakistan stations above 3 km) and there are almost no days of WRF precipitation not shown by the stations (or vice versa). There is thus a correlation of 0.85 between WRF and the stations. The contrast between the Pakistan and Himachal Pradesh stations (particularly above 3 km) in terms of the comparison with WRF suggests that WRF compares much better to observations which more reliably record snowfall. However, a breakdown between rain and snow for the Himachal Pradesh stations and WRF grid points (showing all elevations spanned by the stations) highlights that even with these stations there is a superior comparison for rain than snowfall, in terms of total amount (Fig. 8). The correlation for snowfall (0.81) is in fact higher than for rain (0.63), but WRF consistently shows nearly double the station-measured amount for each day of snowfall. The extent to which this is an overestimate of the model or an underestimate of the stations is uncertain.

The fact that the Pakistan stations above 3 km show so much less winter precipitation than the Himachal Pradesh stations, which measure snow separately (cf. bottom panels of Fig. 7) strongly suggests a significant undercatch of snow. As discussed, the Pakistan stations lie within the area of maximum winter precipitation in High Asia and so should not be showing so much less precipitation than the Himachal Pradesh stations. The superior comparison in Pakistan between the stations and WRF for lower- than higher-elevation stations is likely due to a much greater component of rainfall, which the rain gauges can measure more accurately.

The existence of glaciers at high elevations (above 4 km) in this region indicates that significant snowfall does occur at high elevations in winter. For example, Batura Glacier in the

Karakoram requires 1000–2000 mm snowfall (snow water equivalent, SWE) per year to be sustained, with 1034 mm precipitation measured in one year (not the same year as the current study) at 4840 m elevation (Batura Investigations Group 1979). Also, in the 1980s, annual precipitation accumulations were recorded on the Biafo Glacier by digging snow pits, and studied by Hewitt et al. (1989) and Wake (1989). At 9 different locations on the glacier, ranging from 4650 to 5660 m elevation over 5 different years, almost all annual-accumulated measurements exceeded 1000 mm, with most measurements either just below or exceeding 2000 mm (see Fig. 3 of Hewitt 2011). From visual inspection of this figure in Hewitt (2011), we calculate the mean of those measurements as about 1400 mm. Since Biafo glacier is very near the Pakistan stations used in this study (Fig. 1c, d), the annual accumulation from WRF was averaged over all grid points within the area shown in Fig. 1d within the elevation range 4650–5660 (the range of elevations measured on Biafo Glacier). The mean annual accumulation from April 2005 through March 2006 simulated by WRF is 1237 mm (99% of which being snow), of which 562 mm was during DJFM. By contrast, Khunjerab, the highest of the Pakistan stations used in this study, which is very close to the Batura Glacier and, at 4440 m, only slightly lower in elevation, recorded 197 mm during the year simulated, of which 37 mm was during DJFM. Although the glacier snowfall measurements were in the 1980s, the very similar magnitudes of WRF in 2005–06 and the glacier snowfall measurements suggest that WRF is in fact much closer than the rain-gauge measurements to the true precipitation amounts at these high elevations.

Although we cannot assert that the model is accurate and the stations are not, the station-to-model comparisons highlight the need for reliable permanent stations measuring daily snowfall in the western Himalaya and Karakoram (the snow-measuring stations in Himachal Pradesh being too far from the area of maximum winter precipitation). Daily measurements are required in order to measure the accumulations from individual storms and gauge whether models are simulating them accurately. Measuring snowfall in the western Himalaya is particularly important because such a large proportion of precipitation falls during the winter and at high elevations, as snow, and so rain gauges are not adequate. Further east along the Himalaya, where almost all precipitation falls during summer (Fig. 5), as rain, rain gauges are much more able to represent precipitation patterns and be reliably compared to simulated amounts, as will be shown in Sect. 7.

7 Diurnal cycle of monsoon precipitation

This section focuses on the monsoon months and WRF's ability to simulate the observed diurnal patterns. Both the

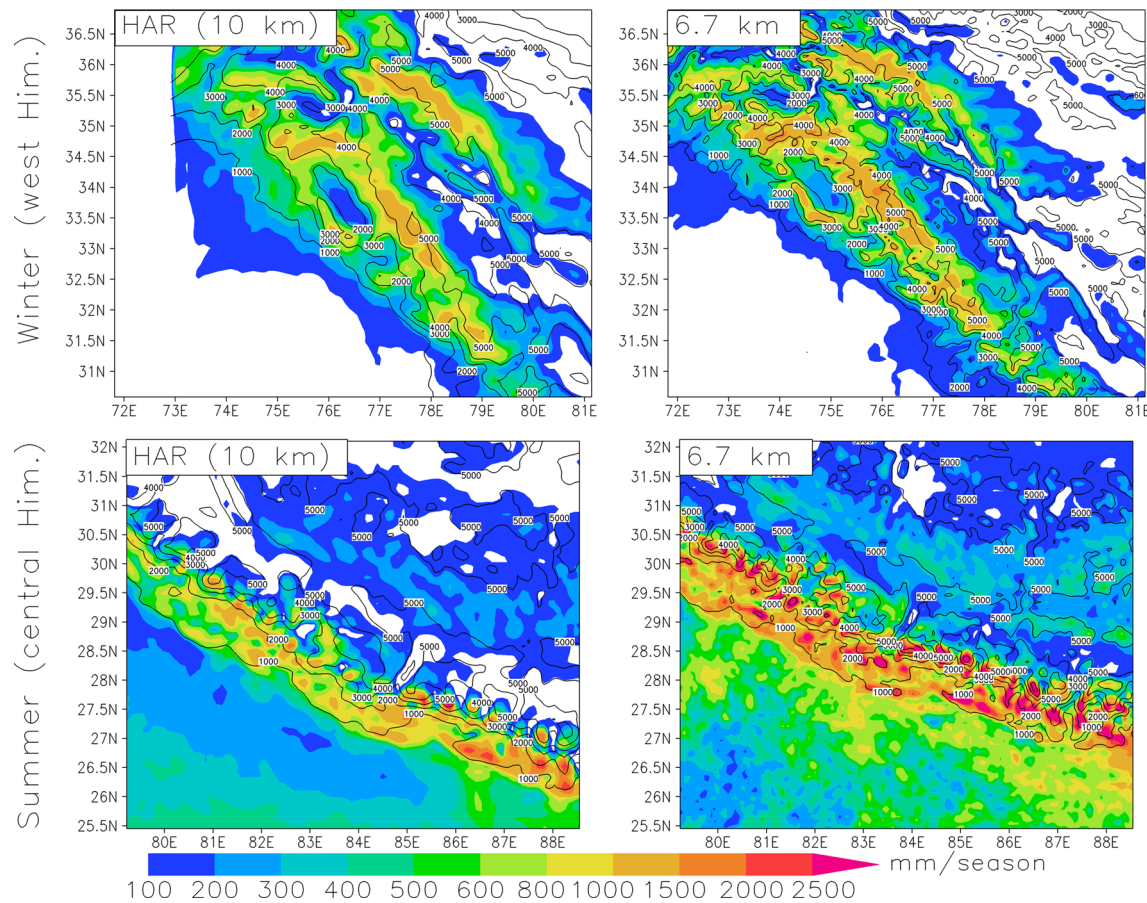


Fig. 4 Total DJFM (*top row*) and JJA (*bottom row*) precipitation (colors, mm) for the year simulated, comparing the 6.7-km simulation and HAR. The areas shown are the western Himalaya and Karakoram for winter (roughly the area of the 2-km winter domain shown

in Fig. 1b) and the central Himalaya (roughly the area of the 2-km summer domain shown in Fig. 1b). Also plotted in all *panels* is elevation from the relevant domain (labeled contours every 1000 m)

station measurements and WRF indicate that, at high elevations during the monsoon, precipitation falls every day (not shown) with a fairly repetitive diurnal cycle. Therefore, the challenge for the model is to simulate accurately the diurnal flow patterns shown by observations and the diurnal evolution of precipitation distribution over the Himalaya. This section compares WRF's diurnal precipitation evolution in the summer months with the available observations—with TRMM and MODIS in terms of how the spatial distribution changes through the day, and also with the high-elevation station measurements in Nepal in terms of the diurnal range of precipitation rate and other atmospheric variables at specific locations.

7.1 Diurnal cycle over the Himalaya

In June–July–August (JJA), a diurnal evolution in precipitation is evident in the WRF simulation, with most 3-h interval precipitation composites correlated above 0.5 with TRMM (Fig. 9). From 0900–2100 (UTC+6, roughly local

time over the whole domain), precipitation is fairly evenly distributed along the full Himalayan range, but from 2100–0900, precipitation becomes more concentrated and intense in the eastern Himalaya. The persistent precipitation across all hours in the eastern Himalaya occurs because the large-scale cyclonic monsoon circulation over northern India remains quasi-stationary and does not undergo any marked diurnal evolution (diagnosed from diurnal composites of low-level winds, not shown). This circulation induces strong southerly moisture advection from the Bay of Bengal against the eastern Himalaya, generating precipitation in that region.

As investigated by Houze et al. (2007) and Medina et al. (2010), monsoon precipitation in the western Himalaya is driven by southwesterly monsoonal flow from the Arabian Sea (just southwest of the area shown in Fig. 9) and undergoes much more of a diurnal evolution than over the eastern Himalaya. Medina et al. (2010) showed that this flow travels about 1000 km over northwest India and, during daytime hours, is subject to strong sensible heat flux

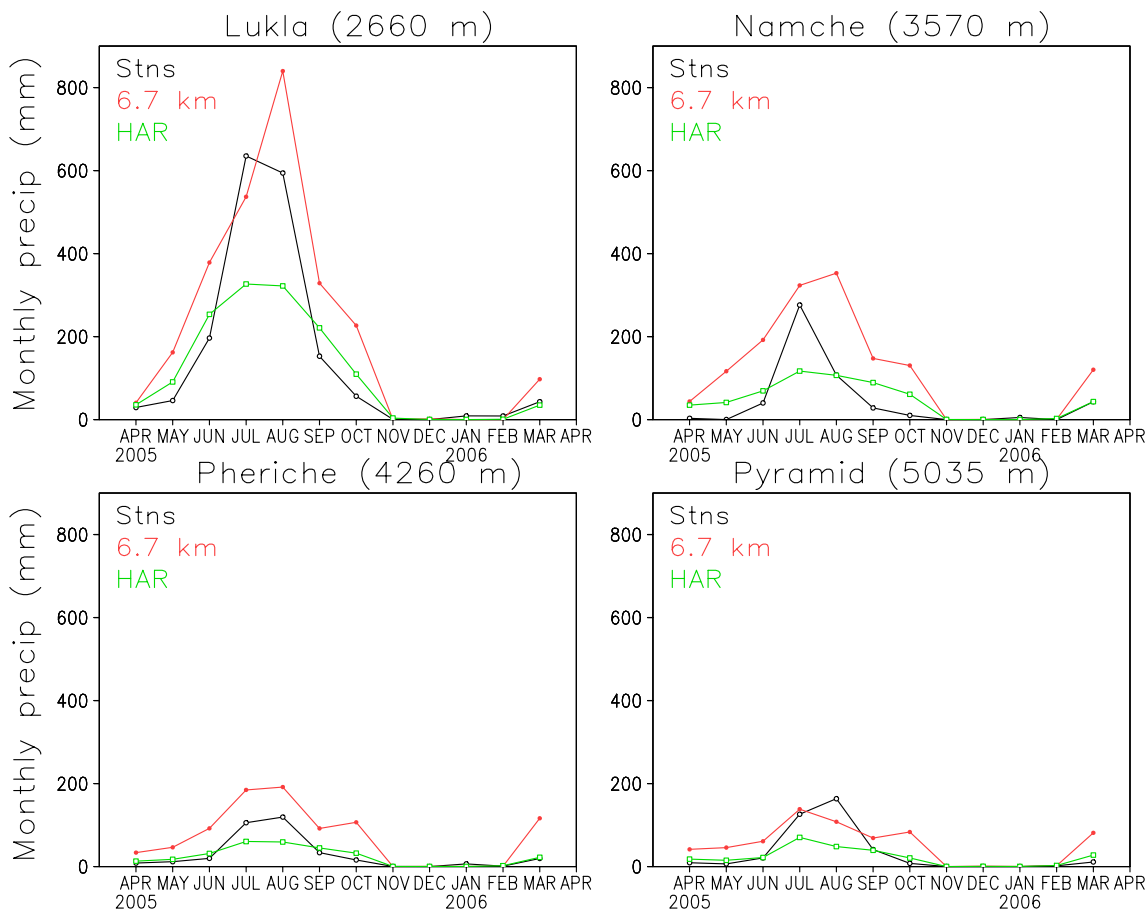


Fig. 5 Time series of monthly-accumulated precipitation at each of the Nepal surface stations, comparing WRF (both the 6.7-km simulation and HAR) to the station measurements, with the simulated val-

ues calculated as detailed in Sect. 3. The locations of the stations are shown in Fig. 1g, h

($>300 \text{ W m}^{-2}$) from the Thar Desert, increasing its buoyancy. Upon reaching the foothills of the western Himalaya, the moisture from this monsoon flow is trapped by the concave orographic barrier formed by the western Himalaya and Hindu Kush, and the foothills trigger intense, relatively small-scale convective cells, which are well represented by the model without a convective parameterization (in particular from 1200 to 1800, Fig. 9).

By contrast, from 2100 to 0900, when precipitation is concentrated in the concave barrier of the eastern Himalaya, this precipitation takes the form of more widespread stratiform convection, reflecting the lack of modification of the monsoonal flow over land. As described by Medina et al. (2010), the southerly flow from the Bay of Bengal generating this precipitation travels over much less land before encountering the orography than the flow from the Arabian Sea that generates precipitation in the western Himalaya. Also, the land over which this air flows is the wetlands of Bangladesh, as opposed to the Thar Desert, so that the flow continues to be subject to strong latent heat

flux. Therefore, the maritime airmass is less modified over land than in the western Himalaya case and there is less of a diurnal signature of precipitation. Consequently, precipitation falls all day in the eastern Himalaya. The nighttime and early morning distribution of precipitation in the eastern Himalaya in Fig. 9 is very similar to Fig. 14 of Medina et al. (2010), which shows the precipitation accumulated in one night in a WRF simulation, and consistent with the diurnal cycle of mesoscale convective systems discussed in Yang et al. (2015). However, although not investigated by Medina et al. (2010), daytime precipitation in the eastern Himalaya is morphologically similar to the intense small-scale convection in the western Himalaya. TRMM also captures this contrast in precipitation morphology in the eastern Himalaya between day and nighttime (not shown). Therefore, daytime heating over Bangladesh is sufficient to form smaller-scale convection. Unlike the intense convection in the western Himalaya, this convection persists into the nighttime as the small-scale convective elements merge and form more widespread convective systems, which are

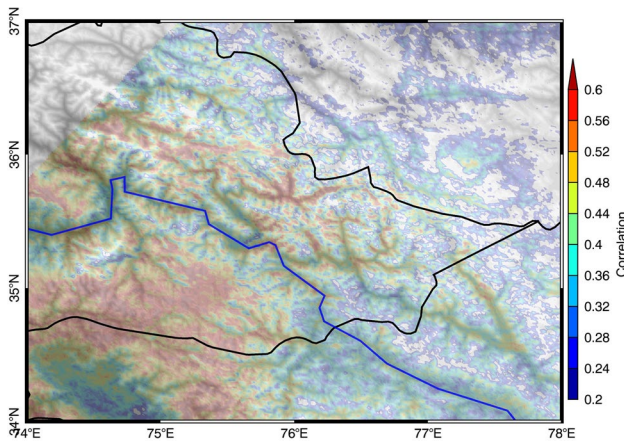


Fig. 6 Pearson product-moment correlation coefficients between daily timeseries of WRF and MODIS cloud fraction (I indicates cloud cover at a given pixel, 0 indicates no cloud cover) from 1 December 2005 to 31 March 2006 over the western Himalaya and Karakoram. The MODIS timeseries is the Cloud Mask product from the daily Aqua pass (about 08 UTC). The WRF timeseries is at 09 UTC each day (the closest output time to the time of the Aqua pass). The given value at each MODIS pixel comes from the temporal correlation at that location, with each MODIS pixel compared to the WRF *grid box* in which it lies. The *blue line* marks the Indus river and the *black lines* indicate international borders

described as persistent convective systems (PECS) in Yang et al. (2015).

During 2100–0900 when precipitation is concentrated further east, the correlation between WRF's and TRMM's precipitation distributions is the best over the diurnal cycle (above 0.6). This is largely because WRF and TRMM agree on a number of locations downslope of major orography where precipitation maxima form (not shown for TRMM). These precipitation maxima occur where the foothills of the eastern Himalaya trigger the large-scale monsoonal flow to form mesoscale convective systems on the slopes of the mountains and on the Meghalaya Plateau (Houze et al. 2007; Medina et al. 2010), which is one of the雨iest places on Earth (Bookhagen et al. 2005; Bookhagen and Burbank 2010). This nocturnal precipitation was also investigated by Sato (2013), who used WRF to identify a summer nocturnal westerly-to-southwesterly low-level jet in the region, which enhanced precipitation from midnight to early morning, particularly in the Himalaya and upwind of the relatively small mountains to the south.

The fact that WRF accurately represents mesoscale convective features that have been identified by previous observational studies is a further testament to its abilities in simulating the region's complex climate. For the same summer, the HAR also shows a near-continuous line of precipitation along the Himalayan range in the afternoon, then becoming more stratiform and concentrated over the eastern part of the domain, as in Fig. 9 (not shown). However, there is a distinctive lack of nocturnal precipitation at high

elevations in the HAR, as is investigated in the following subsection.

7.2 Local mountain and valley diurnal cycles

The analysis in Sect. 7.1 shows that on the scale of the full Himalayan range, WRF simulates diurnal monsoon patterns observed and simulated in previous studies, and shows the same essential diurnal evolution as TRMM. WRF's simulation of the interaction of the monsoon circulation with individual peaks and valleys during the day is now investigated at a scale for which higher-resolution satellite and station data are required for comparison. A much smaller-scale diurnal plot is presented in Fig. 10 in the area indicated by the black boxes in Fig. 9, roughly covering Nepal, showing precipitation and 850-hPa winds every 3 h.

Up to 0900 in JJA, WRF simulates moisture transport along the Himalayan front from east to west as part of the cyclonic monsoon circulation over northern India, as described by Bookhagen et al. (2005). There is widespread precipitation at low elevations, but almost none at high elevations. Then, from 0900, the moisture transport begins to be diverted northward. As captured by the HAR and described by Curio et al. (2015), meridionally oriented valleys channel some of this abundant moisture across the orographic barrier. This effect generates precipitation maxima at each individual mountain top. Pronounced precipitation maxima also form at low elevations, upwind of each mountain peak. Then, after 1800, cross-barrier moisture transport decays and the dominant along-barrier large-scale monsoon circulation resumes. The orographic-forced precipitation maxima thus decay until about 0300.

WRF's build up of convection in the afternoon at high elevations is validated by cloud cover from MODIS during JJA of the summer simulated (Fig. 11). During the summer, meridionally oriented cloud bands along valleys are enhanced from 1100 (the pass of Terra satellite) to 1400 (the pass of Aqua satellite) local time at high elevations (immediately north of the 3-km elevation contour). Cloud enhancement also occurs along high-elevation tributaries north of the 3-km elevation contour. Kurosaki and Kimura (2002) also noted the tendency for the build up of cloud on the windward slopes of the Himalaya during the monsoon from 0900 to 1500. This enhanced cloud cover shown by MODIS verifies the afternoon channeling of moisture up the valleys shown by WRF in Fig. 10. Perhaps the most distinctive afternoon enhancement of cloud cover in Fig. 11 is along the Khumbu Valley (highlighted by the blue box), which is the valley up which the SHARE surface stations in Nepal rise (Fig. 1g). The diurnal evolution in JJA from the perspective of these stations is very similar to WRF for temperature, meridional wind speed, specific humidity, and incoming shortwave radiation (Fig. 12).

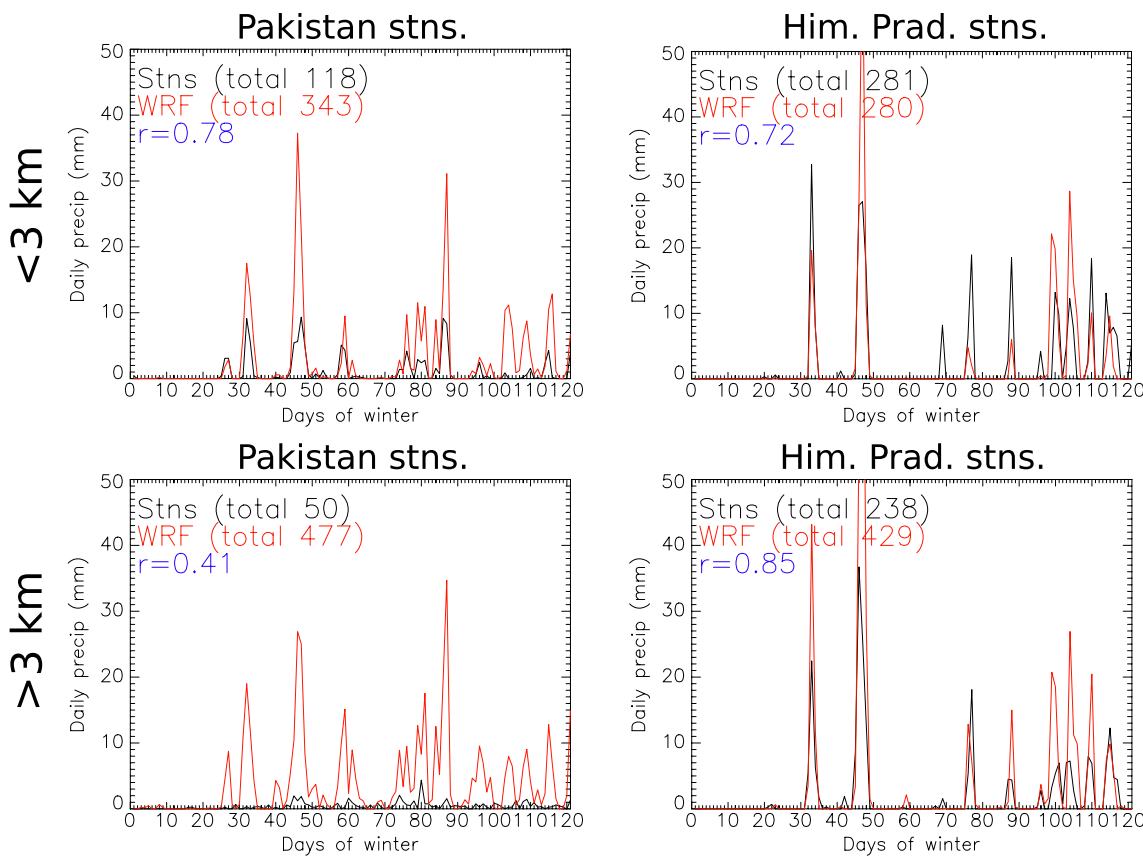


Fig. 7 Time series through winter (1 December–31 March) of daily precipitation for the Pakistan (left column) and Himachal Pradesh (right column) stations, comparing the 6.7-km WRF simulation with the station measurements. For the station timeseries, the mean is calculated of all stations above or below 3 km in Pakistan or Himachal Pradesh (see Table 2). For the WRF timeseries, the mean is calculated of all grid points above or below 3-km elevation in the area covered by the Pakistan (the area plotted in Fig. 1d) or Himachal Pradesh (the

area plotted in Fig. 1f). However, for the below-3-km timeseries, only grid points above the elevation of the lowest station were averaged, and for the above-3-km timeseries, only grid points below the elevation of the highest station were averaged. For each panel, the total accumulation is shown for both WRF and the stations over the time period plotted, as well as the Pearson product-moment correlation coefficient of the two timeseries

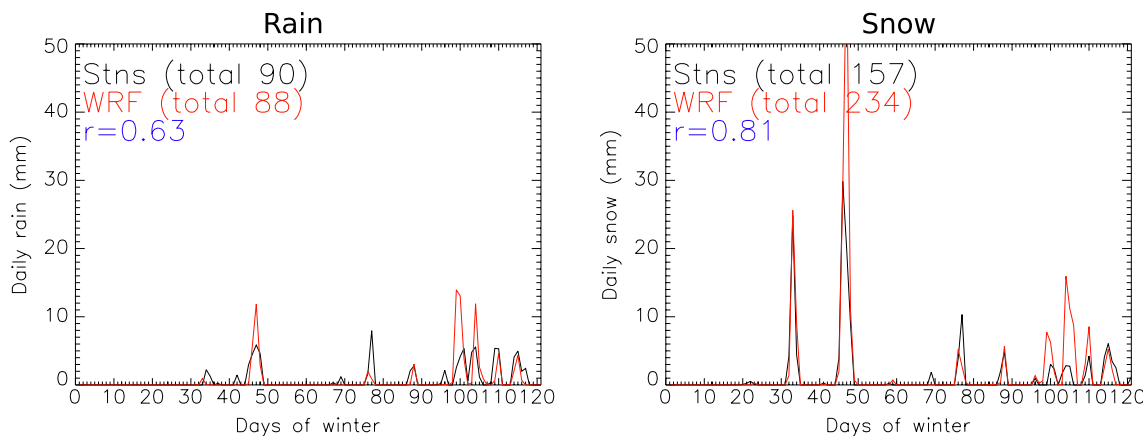


Fig. 8 As Fig. 7, but just for the Himachal Pradesh stations and showing the mean of all stations and, for WRF, the mean of all grid points in the range between the lowest- and highest-elevation stations. Separate time series are shown for rain and snow

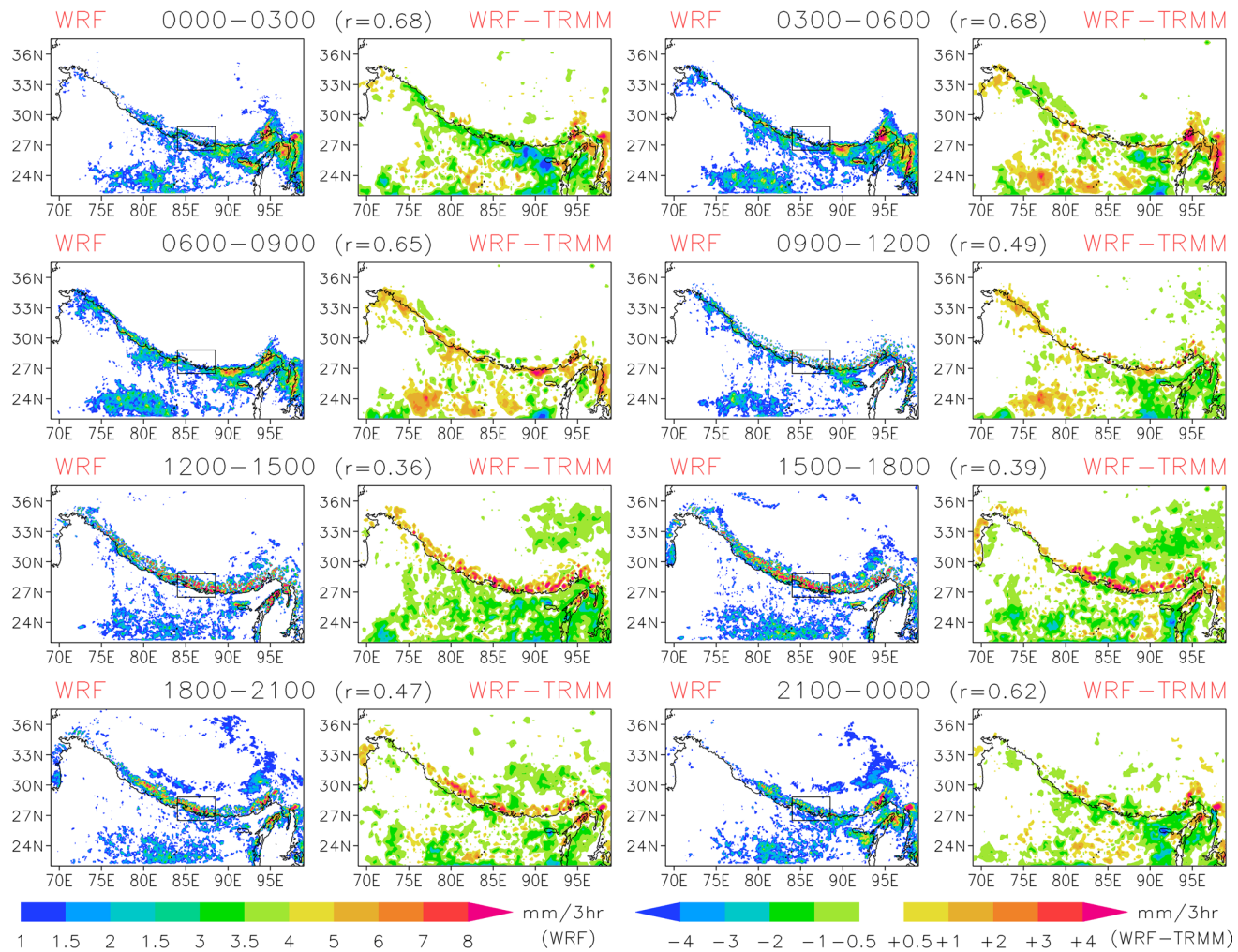


Fig. 9 Composites of 3-h accumulated precipitation for each of the given time intervals in JJA. First and third columns show WRF precipitation, second and fourth columns show TRMM subtracted from WRF rainfall (bilinearly interpolated onto the coarser TRMM grid). The given times of day are UTC+6, which is roughly local time over the whole domain. The given “*r*” values are, for each 3-h period, the

Pearson product-moment correlation coefficient of the spatial distribution of total TRMM and interpolated WRF rainfall, as for the monthly-precipitation maps in Fig. 3. Equivalent correlations but comparing WRF total precipitation are marginally lower. Also plotted in all panels is the 1-km elevation contour. The smaller boxes drawn in the WRF panels show the location of the finer-scale plots in Fig. 10

Although there are slight differences in the magnitudes of some variables at some locations, WRF is almost exactly in sync with the stations in terms of the diurnal cycles. In particular, the afternoon maxima of southerly wind speed and moisture content illustrate the channeling of moisture from low elevations.

Although the Himalayan peaks show the strong afternoon maximum precipitation, in the valleys, the precipitation maximum in fact occurs at nighttime. As described by Barros and Lang (2003), the daytime upslope flow enhances moisture content and convectively available potential energy (CAPE), leading to a secondary rainfall peak. However, in the absence of strong convergence, much of the advected moisture is carried over the mountains. At nighttime, when the upslope flow decays, convergence

is enhanced at the foot of the mountains. Combined with the high moisture and CAPE that has been building in the mountains during the day, this leads to the greatest rainfall around midnight. The Nepal stations in the Khumbu Valley show this nocturnal precipitation maximum during the summer simulated in this study (with an almost identical diurnal cycle to that shown by Barros and Lang 2003, i.e., with a maximum at midnight, their Fig. 2b), but WRF does not in this location, neither in the 6.7-km simulation, nor in the HAR (Fig. 13—the given values are the 3-h accumulation up to the given times on the *x*-axis). However, the 6.7-km domain does show a nocturnal maximum in other valleys nearby (Fig. 14, which shows the 3-h period in which each grid point receives its diurnal precipitation maximum). Nocturnal maxima are particularly evident in

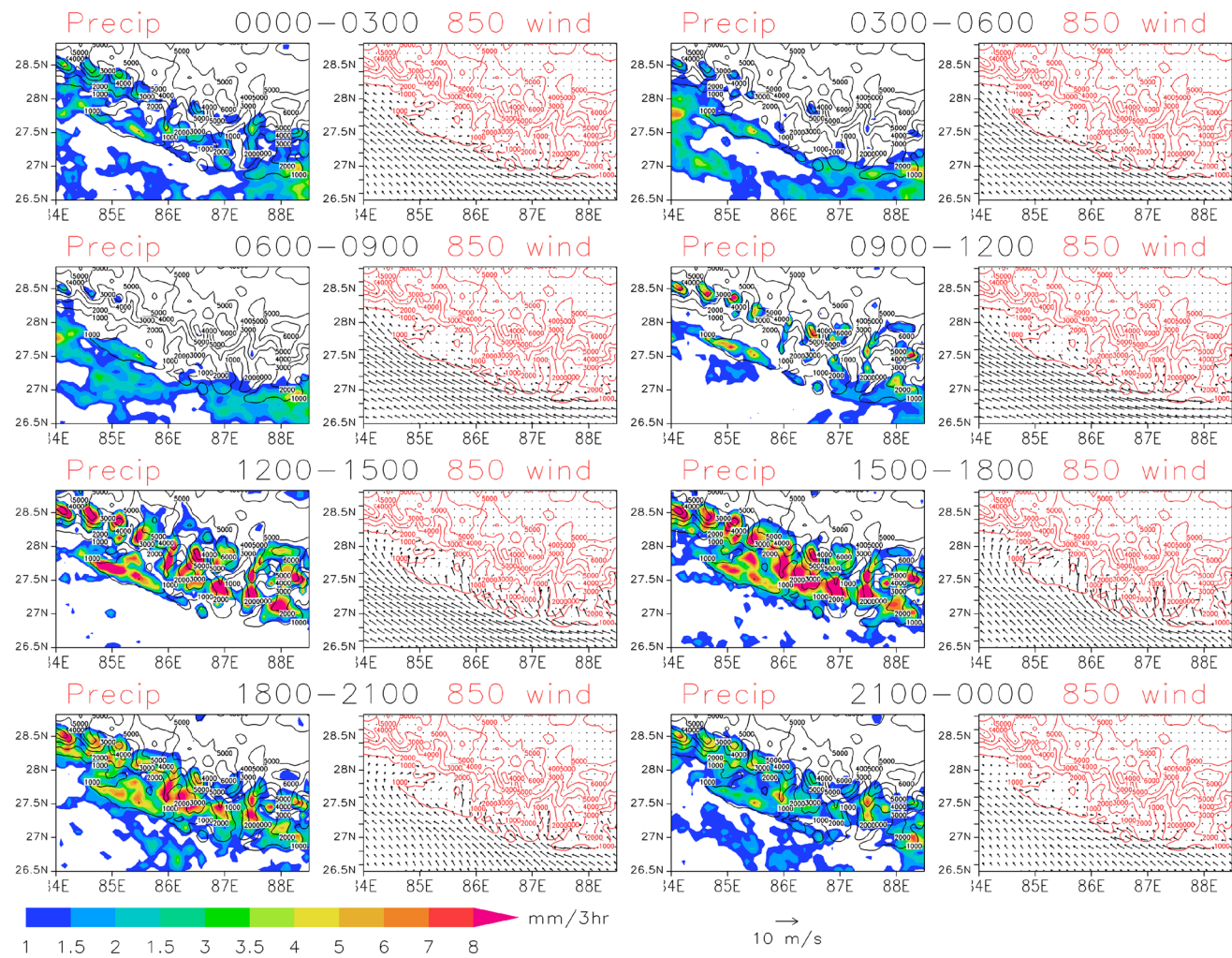


Fig. 10 First and third columns: As Fig. 9, but in the smaller area indicated in Fig. 9. Second and fourth columns: JJA composites of 850-hPa winds (m s^{-1}) over the same area at the beginning of the

given time interval, e.g., the pair of panels labeled 0000–0300 shows precipitation accumulated during those 3 h and winds at 0000. Also plotted in all panels is elevation (labeled contours every 1000 m)

valleys that are inlets into the orogen, which the Khumbu Valley (highlighted by the white box) is not.

WRF shows a strong maximum between 1500 and 1800 in the 6.7-km simulation (and between 1200 and 1500 in the HAR) (Fig. 13) that the stations do not show, before rapidly decreasing into the evening. However, the 6.7-km simulation, particularly at the higher elevations, is fairly well in sync with the stations during the night and early morning. The 6.7-km simulation is also in good agreement with the stations in the rate of decrease of precipitation rate with elevation during these hours (note the difference in scale between panels). Thus, this simulation does capture the nocturnal precipitation cycle, despite a late-afternoon maximum in the Khumbu Valley (Fig. 14) that the stations do not show. The HAR, on the other hand, shows near-zero nocturnal precipitation in the

Khumbu Valley (Fig. 13) or other valleys (not shown). Thus, the apparent overestimate of the 6.7-km simulation of high-elevation summer precipitation, shown as monthly totals in Fig. 5, is due to excessive afternoon precipitation, while the HAR's underestimate is due to a failure to simulate nocturnal precipitation. Therefore, the 6.7-km simulation has a shortcoming during the monsoon in overestimating afternoon convection at high elevations, but otherwise accurately simulates the diurnal cycle at various elevations. The HAR with convective parameterization, on the other hand, does not capture the diurnal pattern in the mountains.

The comparisons in Fig. 13 are at odds with Collier and Immerzeel (2015) whose 5-km domain (their closest grid spacing to ours) underestimated monsoon precipitation over the Himalaya all day (their Fig. 3c). The different

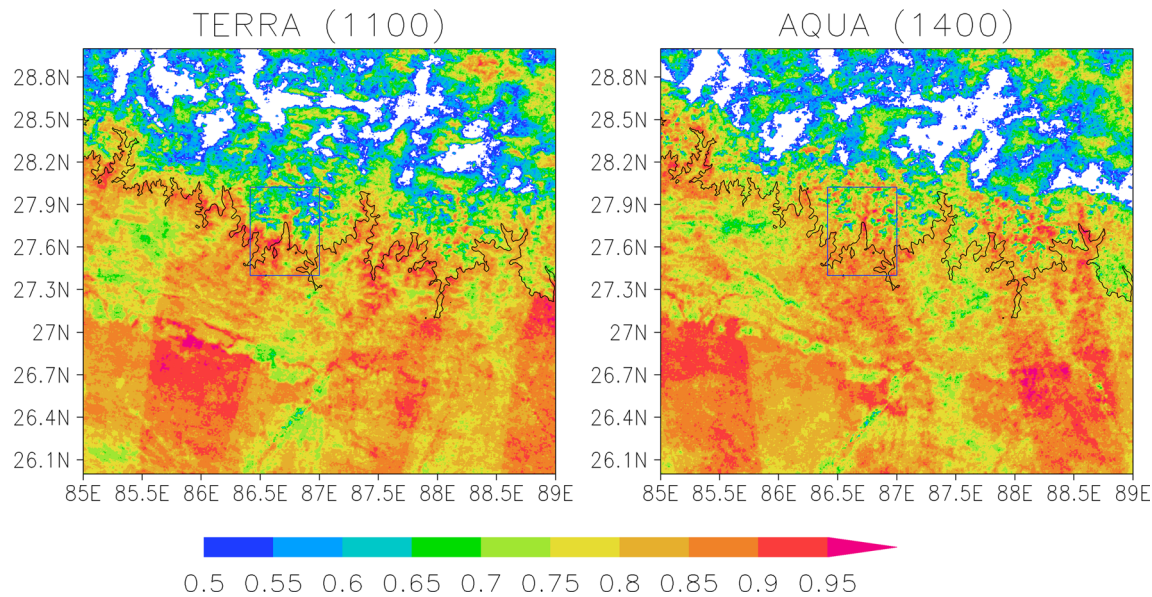


Fig. 11 Mean cloud fraction for JJA from the MODIS Cloud Mask product, comparing the once-daily passes of the Terra and Aqua satellites. The area shown is roughly the same as in Fig. 10. The given times of day are UTC+6 (roughly local time). For a given satellite pass, 1 indicates cloud cover at a given pixel, 0 indicates no cloud

cover. Therefore, the given values are the fraction of days over the summer on which there was cloud at the time of the pass. The 3-km elevation contour is also plotted from SRTM data. The Khumbu Valley is highlighted by a *blue box*, which is where the SHARE stations in Nepal lie (data plotted in Fig. 12)

comparison between WRF and the observations in their study to ours may be because their comparisons were made by taking the nearest WRF grid point to each station's location, whereas the current study compares grid points with similar elevation. In fact, the diurnal cycle of their 1-km domain (which is more likely to match the elevations of the stations) more closely resembles that of our 6.7-km domain, i.e., overestimating in the afternoon and underestimating at night. In this instance, the station measurements are taken to be more accurate than the station measurements shown in winter in Sect. 6 because, even at Pyramid at 5035-m elevation, the mean diurnal temperature is above freezing all day (Fig. 12), hence almost all precipitation falls as rain. Also winds are weaker during the monsoon than during winter storms, so that less undercatch occurs. Because the grid spacing employed in this study is coarse in terms of explicitly resolving convection, the following subsection investigates to what extent this is responsible for the overestimate of afternoon convection in the Himalaya during the monsoon.

7.3 Influence of grid spacing and convective parameterization on monsoon precipitation in the Himalaya

In order to investigate whether the diurnal cycle of monsoon precipitation in the mountains could be simulated more accurately than the model setup employed in this

study is able, different WRF simulations are now compared. A smaller grid spacing, more able to resolve convection explicitly, may be more accurate. Therefore, a third domain of 2.2-km grid spacing was nested within the existing 6.7-km domain at the location shown in Fig. 1b (the “2-km summer” box) for 6 days during the summer, as described in Sect. 2. The accumulation of precipitation in the area covered by the 2.2-km domain is shown in Fig. 15 for the 20, 6.7, and 2.2-km domains for this 6-day simulation. Also shown is the accumulation of precipitation shown by the HAR at 10-km grid spacing during these 6 days. Although there are many higher-resolution features shown in the 2.2-km domain, the distribution shown by the 6.7-km domain is similar to that of the 2.2-km domain. Namely, a maximum in the Himalayan foothills (just south of the 3-km elevation contour in black) is qualitatively very similar between both domains, and lesser maxima lie over individual peaks (just north of the 3-km elevation contour). However, the high-elevation maxima are generally smaller and cover less area in the 2.2 than 6.7-km domain, implying less total precipitation at high elevations.

Mean diurnal cycles of precipitation during this 6-day period are shown in Fig. 16, comparing the 4 domains. These timeseries are obtained by taking the mean of all grid points within two separate areas: 100 km south (<3 km) and 50 km north (>3 km) of the 3-km elevation contour. The bounding lines of the area over which grid points are averaged are shown in red in Fig. 15. These areas are

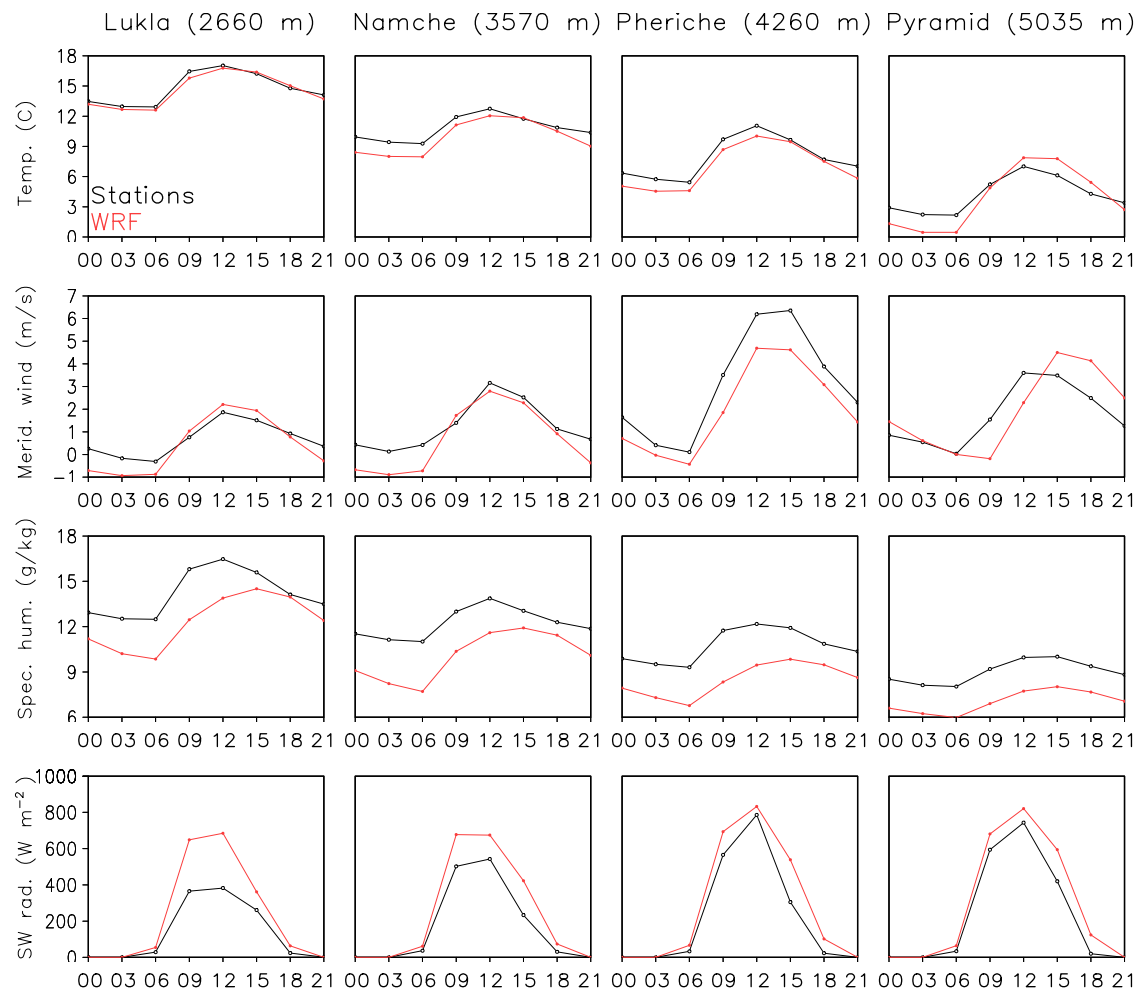


Fig. 12 Diurnal mean timeseries in JJA of temperature, meridional wind speed, specific humidity, and incoming shortwave radiation for each of the surface stations in Nepal, comparing the station measure-

ments and WRF. The given times of day are UTC+6. The locations of the stations are shown in Fig. 1g, h

taken as a proxy for the Himalayan foothills (<3 km) and the windward high elevations (>3 km). As in Fig. 13, the given times of day show the 3-h accumulation up to that time. For both the foothills and high elevations, the 20-km domain and HAR are similar (those with convective parameterization), while the 6.7 and 2.2-km domains (those with no convective parameterization) are similar. In the foothills, the 6.7 and 2.2-km domains show near-constant precipitation with a slight maximum in the early morning, while the 20 and 10-km domains show a strong early-afternoon maximum with very little falling at night or in the morning. At high elevations, all 4 domains show an afternoon maximum, but the 6.7 and 2.2-km domains show about 2 mm per 3 h (a very high rain rate considering this is the average over a large area) persisting through the night. Conversely, the coarser domains show a rapid decrease of precipitation rate in the late afternoon and early evening, with near zero

through the night. In the coarse domains, there is in fact little difference in the diurnal monsoon cycle between the foothills and high elevations, which as documented in previous studies and discussed in Sect. 7.1, is not the case in reality.

The reduction of accumulated high-elevation precipitation in the 2.2-km, relative to 6.7-km, domain (Fig. 15) is largely due to a reduction of the afternoon maximum (Fig. 16, right panel). For these 6 days, the 2.2-km domain reduces this maximum in the 6.7-km domain by about a third. From Fig. 13, this would still imply an overestimate of high-elevation afternoon precipitation, according to the stations, and the 2.2-km domain also fails to show the nocturnal maximum. However, without having simulated a full monsoon season at 2.2-km grid spacing, we cannot say for certain how it would compare to the stations in Nepal. Therefore, decreasing the grid spacing from 6.7 to 2.2 km

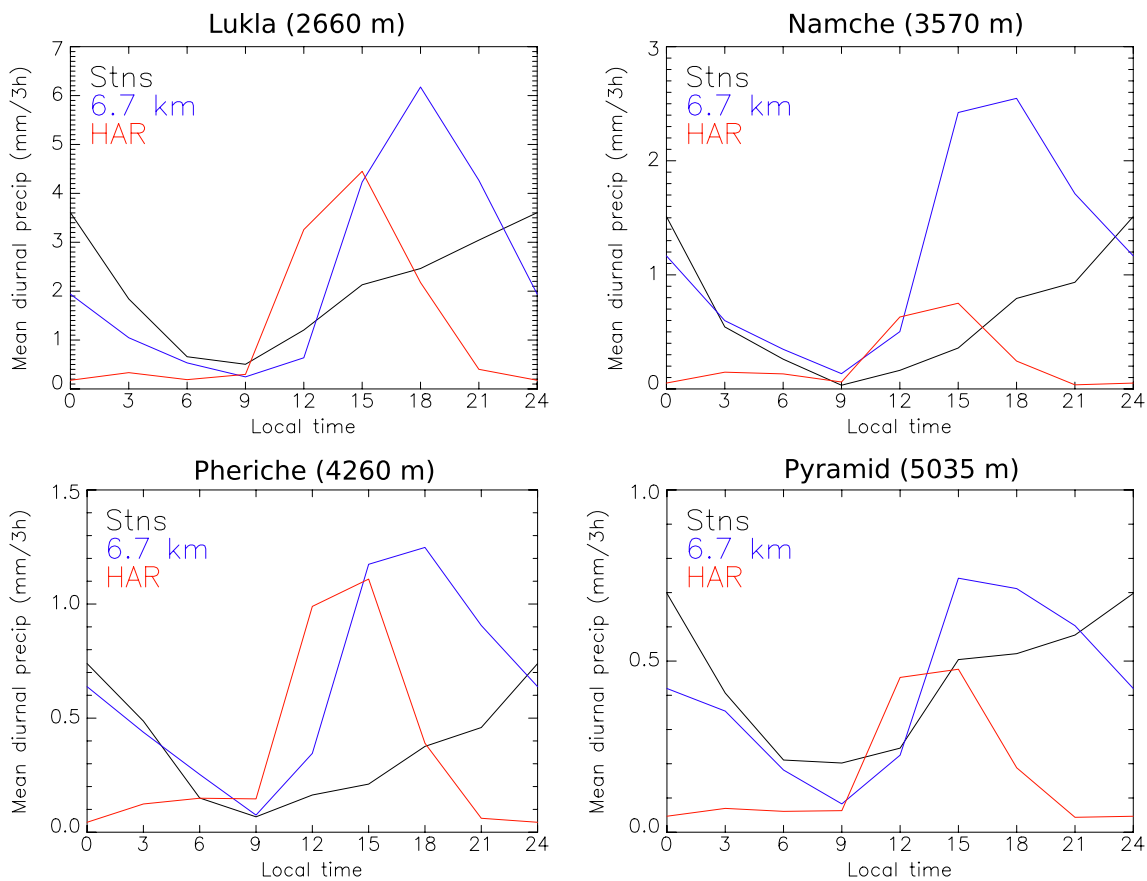
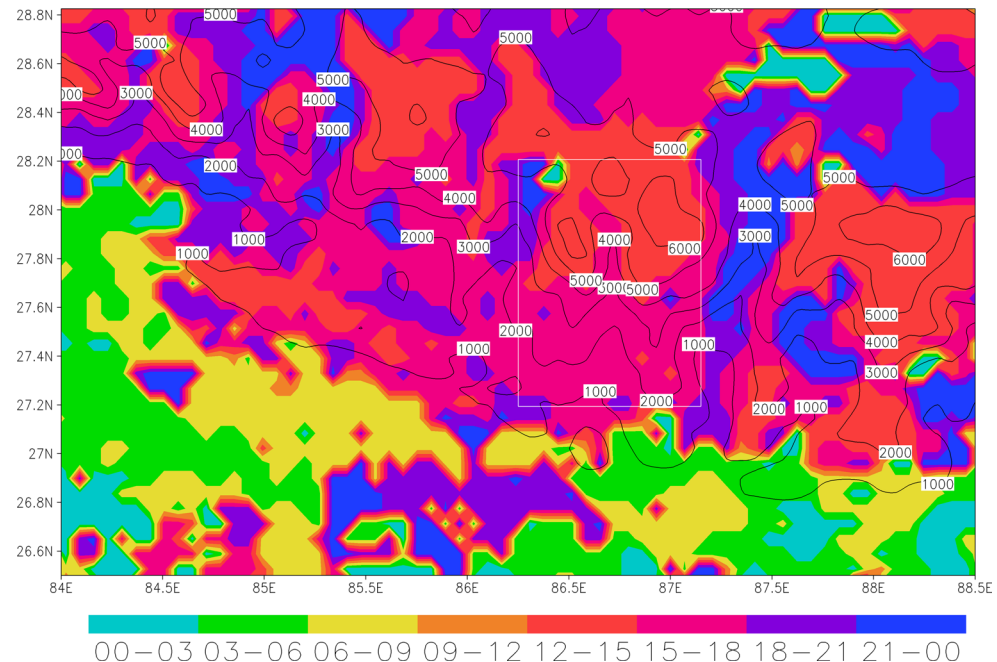


Fig. 13 As Fig. 12, but just showing 3-h accumulated precipitation, comparing WRF (both the 6.7-km simulation and HAR) to the station measurements. The given values represent the accumulation in the 3 h

up to the given time (e.g., the value at 0 local time is the accumulation from 21 to 00)

Fig. 14 A spatial map over Nepal for the 6.7-km domain of the 3-h period (UTC+6) in which the diurnal maximum of precipitation falls during JJA. Labeled contours of elevation are also plotted every 1000 m. The Khumbu Valley containing the SHARE stations is highlighted by the white box



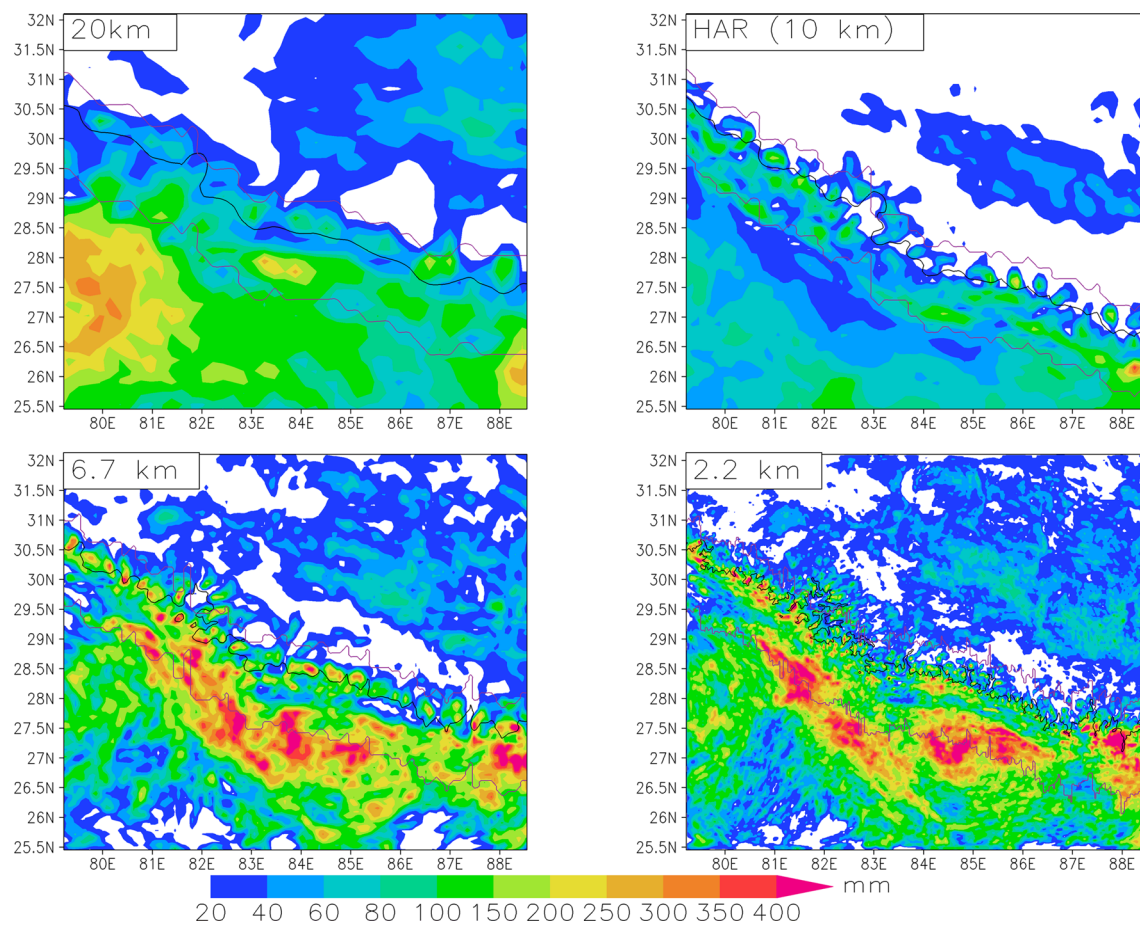


Fig. 15 Accumulated precipitation over 6 days in a separate WRF simulation from 00 UTC 16 July to 00 UTC 22 July 2005 (i.e., within the full year simulated in this study) with three WRF domains shown in Fig. 1 (20, 6.7, and 2.2-km, where the 20 and 6.7-km domains are the same as for the full year's simulation). The accumulation in the HAR over the same time period is also given. The 3-km elevation contour in the relevant domain is also plotted in black. The *pink contours* either side are obtained by, for each x co-ordinate, moving 100 km south and 50 km north (rounding up to the nearest multiple of the

relevant grid spacing) of the 3-km elevation contour in the relevant domain. For x co-ordinates where the 3-km elevation contour passes through multiple y co-ordinates, the southernmost y co-ordinate was selected (so that in some cases the northernmost pink contour intersects the 3-km elevation contour). The areas bound by these contours south and north of the 3-km elevation contour are taken as a proxy for the Himalayan foothills and windward Himalayan high elevations, respectively, and are used for the time series shown in Fig. 16

likely improves the simulation of monsoon mountain precipitation but does not fundamentally change the diurnal pattern. The critical change from low to high resolution is when a grid spacing is employed that does not require convective parameterization. However, it should be noted that both the 20-km domain and the HAR use the Kain-Fritsch cumulus scheme and other schemes may perform better, which this study has not investigated. Regardless, although the 6.7-km grid spacing employed in this study is at the very coarse end of the scale of grid spacings for which convective parameterization may be switched off, it captures the essential diurnal pattern, as well as the rate of reduction of precipitation with elevation (Fig. 13). Given computational constraints, future studies may use such a grid spacing to investigate monsoon precipitation over

the Himalaya, appreciating that afternoon precipitation is overestimated.

8 Summary and conclusions

A WRF simulation was performed for a full 12-month period (April 2005 through March 2006) at 6.7-km grid spacing to investigate inter-seasonal, intra-seasonal, and diurnal precipitation cycles over the Himalaya. April-through-March was chosen in order to simulate full uninterrupted winter and summer seasons, and the particular year selected was very close to average in terms of regional-scale circulation (according to reanalyses) and precipitation (according to satellite estimates of precipitation (TRMM)).

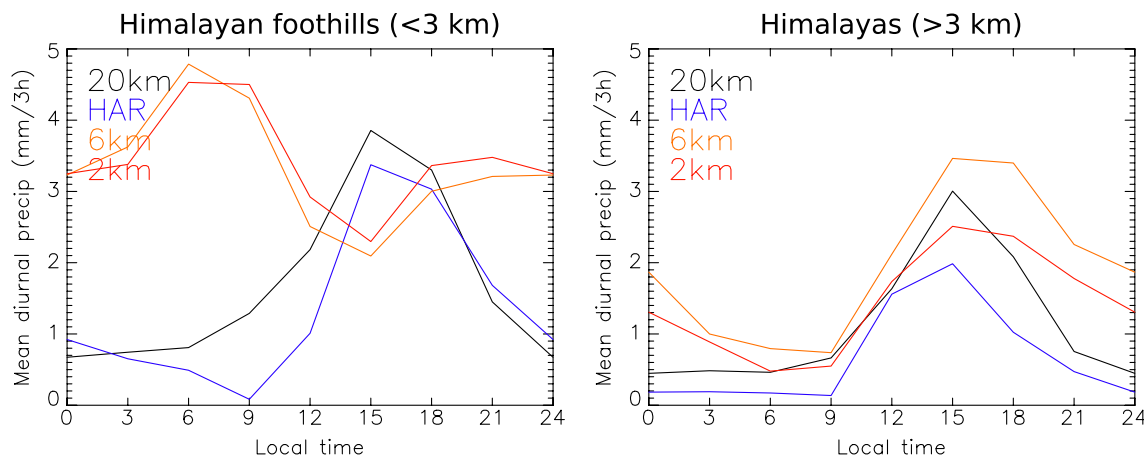


Fig. 16 Timeseries of diurnal mean 3-h precipitation from 16–22 July in the 3-domain simulation shown in Fig. 15, comparing the 3 domains, as well as the HAR over the same time period. For each domain, separate timeseries are shown for the Himalayan foothills (from the mean of all grid points 100 km south of the 3-km eleva-

tion contour) and the windward Himalayan high elevations (from the mean of all grid points 50 km north of the 3-km elevation contour), as detailed in the caption of Fig. 15. For the 20, 6.7-km, and HAR domains, only grid points within the area covered by the 2.2-km domain (plotted in Fig. 15) were considered

When compared to the mean of high-elevation surface stations in Pakistan and Himachal Pradesh, WRF's daily precipitation timeseries through winter is very well correlated with that of the stations. Therefore, WRF is skilful in the timing and relative intensity of precipitation from extratropical cyclones. However, at particularly high elevations, where all winter precipitation falls as snow, WRF shows far greater daily and total-winter accumulations than the stations, but this discrepancy is reduced for stations that estimate snowfall amount from snow depth and density. Although we cannot say for sure that the model is more accurate than the stations, these comparisons highlight the need for reliable permanent stations measuring daily snowfall in the western Himalaya and Karakoram (where almost all winter precipitation falls in the region).

For winter precipitation, the resolution employed in this study is not required to capture the essential precipitation patterns. Coarser simulations show no fundamental difference in the distribution or timing of winter precipitation, with a maximum between 5000 and 5500 m elevation and no difference in the breakdown between rain and snow. There are just slightly lower precipitation magnitudes in coarser simulations on account of less steep slopes. However, for summer precipitation, the nocturnal precipitation in the foothills and valleys of the Himalaya requires an explicit resolution of convection. Although very coarse in terms of resolving convection, the 6.7-km simulation's diurnal precipitation cycle is mostly well in sync with that of station measurements from 2660–5035-m elevation in Nepal. The only discrepancy is in the afternoon when WRF shows a large daily maximum not shown by the stations. A

shorter simulation with a 2.2-km domain nested shows no fundamental difference to the 6.7-km domain in the diurnal cycle of precipitation, but shows a reduction of this afternoon maximum in the 6.7-km domain by about a third. Therefore, the 6.7-km grid spacing employed in this study is appropriate for investigating the diurnal cycle of monsoon precipitation over the Himalaya, but appears to overestimate afternoon precipitation at high elevations.

This study serves as an overview of the ability of WRF to simulate accurately the spatiotemporal distribution of precipitation on the mesoscale, arising from the interaction of various weather systems with the Himalaya and throughout seasons. These analyses provide a greater understanding of the reliability and limitations of WRF simulations that can be useful to investigate climate change in High Asia and thus predict future water resources in south Asia at the regional scale.

Acknowledgements This research was supported by the Climate and Large-scale Dynamics Program, from the National Science Foundation (NSF award-AGS 1116105) and by the U.S. National Aeronautics and Space Administration (NASA) Headquarters under the NASA Earth and Space Science Fellowship Program (Grant Number 13-EARTH13F-26). The CFSR data used in this research were developed by NCEP and provided by the National Center for Atmospheric Research (NCAR), available at <http://rda.ucar.edu/pub/cfsr.html>. TRMM data were acquired by an international joint project sponsored by the Japan National Space Development Agency (NASDA) and the NASA Office of Earth Science, available at <http://trmm.gsfc.nasa.gov>. High-performance computing support from Yellowstone (ark:/85065/d7wd3xhc) was provided by NCAR's Computational and Information Systems Laboratory (CISL), sponsored by the NSF. Thanks to the anonymous reviewers whose comments have greatly improved our manuscript.

References

- Anders AM, Roe GH, Hallet B, Montgomery DR, Finnegan NJ, Putkonen J (2006) Spatial patterns of precipitation and topography in the Himalaya. *Geol Soc Am Spec Pap* 398:39–53
- Archer DR, Fowler HJ (2004) Spatial and temporal variations in precipitation in the Upper Indus Basin, global teleconnections and hydrological implications. *Hydrol Earth Syst Sci* 8:47–61
- Bao X, Zhang F (2013) Evaluation of NCEP-CFSR, NCEP-NCAR, ERA-Interim, and ERA-40 reanalysis datasets against independent sounding observations over the Tibetan Plateau. *J Clim* 26:206–214
- Barlow M, Wheeler M, Lyon B, Cullen H (2005) Modulation of daily precipitation over southwest Asia by the Madden-Julian Oscillation. *Mon Weather Rev* 133:3579–3594
- Barnett TP, Adam JC, Lettenmaier DP (2005) Potential impacts of a warming climate on water availability in snow-dominated regions. *Nature* 438:303–309
- Barros AP, Lang TJ (2003) Monitoring the monsoon in the Himalayas: observations in central Nepal, June 2001. *Mon Weather Rev* 131:1408–1427
- Barros AP, Chiao S, Lang TJ, Burbank D, Putkonen J (2006) From weather to climate-seasonal and interannual variability of storms and implications for erosion processes in the Himalaya. *Geol Soc Am Spec Pap* 398:17–38
- Bollasina M, Bertolani L, Tartari G (2002) Meteorological observations at high altitude in the Khumbu Valley, Nepal Himalayas, 1994–1999. *Bull Glaciol Res* 19:1–11
- Bonasoni P, Laj P, Angelini F, Arduini J, Bonafè U, Calzolari F, Cristofanelli P, Decesari S, Facchini MC, Fuzzi S, Gobbi GP, Maione M, Marinoni A, Petzold A, Roccato F, Roger JC, Sellegrí K, Sprenger M, Venzac H, Verza GP, Villani P, Vuillermoz E (2008) The ABC-Pyramid Atmospheric Research Observatory in Himalaya for aerosol, ozone and halocarbon measurements. *Sci Total Environ* 391:252–261
- Bookhagen B, Thiede RC, Strecker MR (2005) Abnormal monsoon years and their control on erosion and sediment flux in the high, arid northwest Himalaya. *Earth Planet Sci Lett* 231:131–146
- Bookhagen B, Burbank DW (2006) Topography, relief, and TRMM-derived rainfall variations along the Himalaya. *Geophys Res Lett* 33:L08405. doi:[10.1029/2006GL026037](https://doi.org/10.1029/2006GL026037)
- Bookhagen B, Burbank DW (2010) Towards a complete Himalayan hydrological budget: the spatiotemporal distribution of snowmelt and rainfall and their impact on river discharge. *J Geophys Res* 115:F03019
- Collier E, Immerzeel WW (2015) High-resolution modeling of atmospheric dynamics in the Nepalese Himalaya. *J Geophys Res* 120(19):9882–9896
- Cannon F, Carvalho LMV, Jones C, Hoell A, Norris J, Kiladis GN, Tahir AA (2016) The influence of tropical forcing on extreme winter precipitation in the western Himalaya. *Dyn Clim.* doi:[10.1007/s00382-016-3137-0](https://doi.org/10.1007/s00382-016-3137-0)
- Carvalho LMV, Jones C, Cannon F, Norris J (2016) Intraseasonal-to-interannual variability of the Indian monsoon identified with the Large-scale Index for the Indian Monsoon System (LIMS). *J Clim* 29:2941–2962
- Curio J, Maussion F, Scherer D (2015) A 12-year high-resolution climatology of atmospheric water transport over the Tibetan Plateau. *Earth Syst Dyn* 6:109–124
- Dimri AP, Chevaturi A (2014) Model sensitivity analysis study for western disturbances over the Himalayas. *Meteorol Atmos Phys* 123:155–180
- Fowler HJ, Archer DR (2006) Conflicting signals of climate change in the Upper Indus Basin. *J Clim* 19:4276–4293
- Ghimire S, Choudhary A, Dimri AP (2015) Assessment of the performance of CORDEX-South Asia experiments for monsoonal precipitation over the Himalayan region during present climate: part I. *Dyn Clim.* doi:[10.1007/s00382-015-2747-2](https://doi.org/10.1007/s00382-015-2747-2)
- Hewitt K, Wake CP, Young GJ, David C (1989) Hydrological investigations at Biafo Glacier, Karakoram Himalaya: an important source of water for the Indus River. *Ann Glaciol* 13:103–108
- Hewitt K (2011) Glacier change, concentration, and elevation effects in the Karakoram Himalaya, Upper Indus Basin. *Mt Res Dev* 31:188–200
- Hewitt K (2014) Glaciers of the Karakoram Himalaya: Glacial environments, processes, hazards and resources. Springer, Dordrecht
- Hong S-Y, Noh Y, Dudhia J (2006) A new vertical diffusion package with an explicit treatment of entrainment processes. *Mon Weather Rev* 134:2318–2341
- Houze RA Jr, Wilton DC, Smull BF (2007) Monsoon convection in the Himalayan region as seen by the TRMM precipitation radar. *Q J R Meteorol Soc* 133:1389–1411
- Huffman GJ, Adler RF, Bolvin DT, Gu G, Nelkin EJ, Bowman KP, Hong Y, Stocker EF, Wolff DB (2007) The TRMM multisatellite precipitation analysis (TMPA): quasi-global, multiyear, combined-sensor precipitation estimates at fine scales. *J Hydrometeorol* 8:38–55
- Iacono MJ, Delamere JS, Mlawer EJ, Shephard MW, Cloud SA, Collins WD (2008) Radiative forcing by long-lived greenhouse gases: calculations with the AER radiative transfer models. *J Geophys Res* 113:D13103, 8
- Immerzeel WW, Bierkens MFP (2012) Asia's water balance. *Nat Geosci* 5:841–842
- Immerzeel WW, Pellicciotti F, Bierkens MFP (2013) Rising river flows throughout the twenty-first century in two Himalayan glacierized watersheds. *Nat Geosci* 6:742–745
- Jones C (2009) A homogeneous stochastic model of the Madden Julian oscillation. *J Clim.* 22:3270–3288
- Kain JS (2004) The Kain-Fritsch convective parameterization: an update. *J Appl Meteorol* 43:170–181
- Kapnick SB, Delworth TL, Ashfaq M, Malyshev S, Milly PCD (2014) Snowfall less sensitive to warming in Karakoram than in Himalayas due to a unique seasonal cycle. *Nat Geosci* 7:834–840
- Kurosaki Y, Kimura F (2002) Relationship between topography and daytime cloud activity around Tibetan Plateau. *J Meteorol Soc Jpn* 80:1339–1355
- Lang TJ, Barros AP (2004) Winter storms in the Central Himalayas. *J Meteorol Soc Jpn* 82:829–844
- Li M, Ma Y, Hu Z, Ishikawa H, Oku Y (2009) Snow distribution over the Namco lake area of the Tibetan Plateau. *Hydrol Earth Syst Sci* 13:2023–2030
- Lutz AF, Immerzeel WW, Shrestha AB, Bierkens MFP (2014) Consistent increase in High Asia's runoff due to increasing glacier melt and precipitation. *Nat Clim Change* 4:587–592
- Maussion F, Scherer D, Finkelnburg R, Richters J, Yang W, Yao T (2011) WRF simulation of a precipitation event over the Tibetan Plateau, China: an assessment using remote sensing and ground observations. *Hydrol Earth Syst Sci* 15:1795–1817
- Maussion F, Scherer D, Mölg T, Collier E, Curio J, Finkelnburg R (2014) Precipitation seasonality and variability over the Tibetan Plateau as resolved by the High Asia Reanalysis. *J Clim* 27:1910–1927
- Medina S, Houze RA Jr, Kumar A, Niyogi D (2010) Summer monsoon convection in the Himalayan region: terrain and land cover effects. *Q J R Meteorol Soc* 136:593–616
- Monin AS, Obukhov AM (1954) Basic laws of turbulent mixing in the surface layer of the atmosphere. *Tr Akad Nauk SSSR Geofiz Inst* 24(151):163–187
- Niu G-Y, Yang Z-L, Mitchell KE, Chen F, Ek MB, Barlage M, Kumar A, Manning K, Niyogi D, Rosero E, Tewari M, Xia Y (2011) The community Noah land surface model with multiparameterization

- options (NoahMP): 1. Model description and evaluation with localscale measurements. *J Geophys Res* 116:D12109, 19
- Norris J, Carvalho LMV, Jones C, Cannon F (2015) WRF simulations of two extreme snowfall events associated with contrasting extra-tropical cyclones over the western and central Himalaya. *J Geophys Res* 120:3114–3138
- Palazzi E, Tahir AA, Cristofanelli P, Vuillermoz E, Provenzale A (2015) Climatic characterization of Baltoro Glacier (Karakoram) and northern Pakistan from in-situ stations. *Eng Geol Soc Territ* 1:33–37
- Putkonen JK (2004) Continuous snow and rain data at 500–4400 m altitude near Annapurna, Nepal, 1999–2001. *Arct Antarct Alp Res* 36(2):244–248
- Rasmussen R, Liu C, Ikeda K, Gochis D, Yates D, Chen F, Tewari M, Barlage M, Dudhia J, Yu W, Miller K (2011) High-resolution coupled climate runoff simulations of seasonal snowfall over Colorado: a process study of current and warmer climate. *J Clim* 24:3015–3048
- Saha S, Moorthi S, Pan H-L, Wu X, Wang J, Nadiga S, Tripp P, Kistler R, Woollen J, Behringer D, Liu H, Stokes D, Grumbine R, Gayno G, Wang J, Hou Y-T, Chuang H-Y, Juang H-MH, Sela J, Iredell M, Treadon R, Kleist D, Van Delst P, Keyser D, Derber J, Ek M, Meng J, Wei H, Yang R, Lord S, van den Dool H, Kumar A, Wang W, Long C, Chelliah M, Xue Y, Huang B, Schemm J-K, Ebisuzaki W, Lin R, Xie P, Chen M, Zhou S, Higgins W, Zou C-Z, Liu Q, Chen Y, Han Y, Cucurull L, Reynolds RW, Rutledge G, Goldberg M (2010) The NCEP climate forecast system reanalysis. *Bull Am Meteorol Soc*, pp 1015–1057. doi:[10.1175/2010BAMS3001.1](https://doi.org/10.1175/2010BAMS3001.1)
- Sato T, Yoshikane T, Satoh M, Miura H, Fujinami H (2008) Resolution dependency of the diurnal cycle of convective clouds over the Tibetan Plateau in a mesoscale model. *J Meteorol Soc Jpn* 86A:17–31
- Sato T (2013) Mechanism of orographic precipitation around the Meghalaya Plateau associated with intraseasonal oscillation and the diurnal cycle. *Mon Weather Rev* 141:2451–2466
- Scientia Sinica (1979) The Batura Glacier in the Karakoram Mountains and its variations. 22:958–974
- Scherler D, Bookhagen B, Strecker MR (2011) Spatially variable response of Himalayan glaciers to climate change affected by debris cover. *Nat Geosci* 4:156–159
- Skamarock WC, Klemp JB, Dudhia J, Gill DO, Barker DM, Duda MG, Huang X-Y, Wang W, Powers JG (2008) A Description of the Advanced Research WRF Version 3. NCAR Technical Note NCAR/TN-475+STR. NCAR, Boulder, CO
- Stauffer DR, Seaman NL (1990) Use of four-dimensional data assimilation in a limited-area mesoscale model. Part I: experiments with synoptic-scale data. *Mon Weather Rev* 118:1250–1277
- Stauffer DR, Seaman NL, Binkowski FS (1991) Use of four-dimensional data assimilation in a limited-area mesoscale model. Part II: effects of data assimilation within the planetary boundary layer. *Mon Weather Rev* 119:734–754
- Tahir AA, Chevallier P, Arnaud Y, Ahmad B (2011) Snow cover dynamics and hydrological regime of the Hunza River basin, Karakoram Range, Northern Pakistan. *Hydrol Earth Syst Sci* 15:2275–2290
- Thomas L, Dash SK, Mohanty UC (2014) Influence of various land surface parameterization schemes on the simulation of Western disturbances. *Meteorol Appl* 21:635–643
- Thompson G, Field PR, Rasmussen RM, Hall WD (2008) Explicit forecasts of winter precipitation using an improved bulk micro-physics scheme. Part II: implementation of a new snow parameterization. *Mon Weather Rev* 136:5095–5115
- Ueno K, Toyotsu K, Bertolani L, Tartari G (2008) Stepwise onset of monsoon weather observed in the Nepal Himalaya. *Mon Weather Rev* 136:2507–2522
- Vano JA, Udall B, Cayan DR, Overpeck JT, Brekke LD, Das T, Hartmann HC, Hidalgo HG, Hoerling M, McCabe GJ, Morino K, Webb RS, Werner K, Lettenmaier DP (2014) Understanding uncertainties in future Colorado River streamflow. *Bull Am Meteorol Soc*, pp 59–78. doi:[10.1175/BAMS-D-12-00228.1](https://doi.org/10.1175/BAMS-D-12-00228.1)
- Wake CP (1989) Glaciochemical investigations as a tool to determine the spatial variation of snow accumulation in the central Karakoram, northern Pakistan. *Ann Glaciol* 13:279–284
- Wulf H, Bookhagen B, Scherler D (2010) Seasonal precipitation gradients and their impact on fluvial sediment flux in the Northwest Himalaya. *Geomorphology* 118:13–21
- Yang X, Fei J, Huang X, Cheng X, Carvalho LMV, He H (2015) Characteristics of mesoscale convective systems over China and its vicinity using geostationary satellite FY2. *J Clim* 28:4890–4907
- Yasutomi N, Hamada A, Yatagai A (2011) Development of a long-term daily gridded temperature dataset and its application to rain/snow discrimination of daily precipitation. *Glob Environ Res* 15(2):165–172
- Yatagai A, Kamiguchi K, Arakawa O, Hamada A, Yasutomi N, Kitoh A (2012) APHRODITE: constructing a long-term daily gridded precipitation dataset for Asia based on a dense network of rain gauges. *Bull Am Meteorol Soc*, pp 1401–1415. doi:[10.1175/BAMS-D-11-00122.1](https://doi.org/10.1175/BAMS-D-11-00122.1)